Molecular Therapy
Original Article

Discovery of a new selective ERAP1 inhibitor for Hedgehog-dependent cancer treatment

Francesca Bufalieri,[1,12] Antonino Cucinotta,[1,12] Silvia Cammarone,[2,12] Francesca Agnoli,[1] Irene Basili,[1,3,4,5] Giulia Ferri,[1] Deborah Quaglio,[2] Miriam Caimano,[1] Anna Laura Capriotti,[6] Carmela Maria Montone,[6] Ludovica Lospinoso Severini,[1] Patrizia Tempora,[7] Silvia D'Amico,[7] Francesca Juretich,[8] Marta S. Semrau,[9] Shirin Navacci,[1] Marilisa Conenna,[1] Rosa Bordone,[1] Francesco Spallotta,[3,10] Silvia Garavaglia,[8] Paola Storici,[9] Francesca Ghirga,[2] Aldo Laganà,[6] Franco Locatelli,[7] Olivier Ayrault,[4,5] Paola Infante,[1] Bruno Botta,[2] Mattia Mori,[11] Doriana Fruci,[7] and Lucia Di Marcotullio[1,3]

[1]Department of Molecular Medicine, Sapienza University of Rome, 00161 Rome, Italy; [2]Department of Chemistry and Technology of Drugs, Sapienza University of Rome, 00185 Rome, Italy; [3]Istituto Pasteur Italia-Fondazione Cenci Bolognetti, Sapienza University of Rome, 00161 Rome, Italy; [4]Institut Curie, PSL Research University, INSERM U1330/CNRS EMR 8001, Children's Oncology Research Unit (CONCERT), Equipe Labellisée Ligue Contre le Cancer, Orsay, France; [5]Université Paris-Saclay, INSERM U1330/CNRS EMR 8001, Children's Oncology Research Unit (CONCERT), Equipe Labellisée Ligue Contre le Cancer, Orsay, France; [6]Department of Chemistry, Sapienza University of Rome, 00185 Rome, Italy; [7]Bambino Gesù Children's Hospital, IRCCS, 00146 Rome, Italy; [8]Department of Scienze del Farmaco, University of Piemonte Orientale, 28100 Novara, Italy; [9]Protein Targets for Drug Discovery Lab, Elettra Sincrotrone Trieste S.C.p.A, 34149 Basovizza, Trieste, Italy; [10]Department of Biology and Biotechnologies "Charles Darwin", Sapienza University of Rome, 00185 Rome, Italy; [11]Department of Biotechnology, Chemistry, and Pharmacy, University of Siena, 53100 Siena, Italy

Inappropriate activation of the Hedgehog (HH) signaling pathway drives the pathogenesis of several cancers, including medulloblastoma (MB), the most common malignant brain tumor in children. HH group MB (HH-MB) is highly heterogeneous and resistant to current treatments. Understanding the molecular events underlying the control of the HH pathway is critical for the development of more effective and tailored interventions. Endoplasmic reticulum aminopeptidase 1 (ERAP1), a key regulator of the immune response, has emerged as a promising therapeutic target for HH-MB, but the lack of clinically viable ERAP1 inhibitors has hindered progress in this area. Here, we identify canthin-6-one (N1) as a selective ERAP1 inhibitor. N1 binds directly to ERAP1 and disrupts its function in the HH pathway, resulting in reduced signaling. Specifically, N1 impairs the association of ERAP1 with the deubiquitinase USP47, promoting βTrCP protein stability and Gli1 degradation. Notably, HH-dependent cells genetically depleted for ERAP1 are insensitive to N1, confirming its specificity. Remarkably, N1 inhibits HH-MB growth *in vitro* and *in vivo*, crosses the blood-brain barrier, and improves survival in an HH-MB mouse model. These findings highlight N1 as a breakthrough ERAP1 inhibitor and provide a promising therapeutic option for the treatment of HH-dependent cancers.

INTRODUCTION

The Hedgehog (HH) signaling pathway plays a crucial role in embryogenesis and stemness maintenance, and its deregulation has been implicated in a wide range of cancers.[1–5] HH signaling is governed by extracellular HH ligands and two transmembrane receptors, Patched1 (Ptch1) and Smoothened (SMO). The binding of the ligand to its Ptch1 receptor releases repression on the SMO co-receptor, leading to activation of the Gli family transcription factors,[2,6] with Gli1 and Gli2 having activating functions and Gli3 acting mainly as a repressor.[7] Gli regulation is finely orchestrated by ubiquitin-dependent proteolytic processes, including those mediated by the β-transducin-repeat containing E3 ubiquitin protein ligase (βTrCP), an F box protein of the Skp1/Cul1/F box E3-ligase complex. Indeed, βTrCP controls the activation of the HH pathway by promoting the proteasomal degradation of Gli1 and Gli2[8–11] and the cleavage of Gli3 into its repressor form, Gli3R.[12–14] Deregulation of these events leads to uncontrolled cell proliferation and tumorigenesis.[9] Among the HH-dependent tumors, medulloblastoma (HH-MB) is the most common malignant and highly aggressive pediatric brain cancer. HH-MB results from alterations in the developmental program of cerebellar granule neuron progenitors (GNPs), which are mainly mutated in Ptch1 or SMO receptors.[15] Notably, non-canonical activation of the HH pathway is also frequently observed in MB and other tumors, highlighting the importance of

---

Received 11 April 2025; accepted 14 October 2025;
https://doi.org/10.1016/j.ymthe.2025.10.036.

[12]These authors contributed equally

Correspondence: Mattia Mori, Department of Biotechnology, Chemistry, and Pharmacy, University of Siena, 53100 Siena, Italy.
E-mail: mattia.mori@unisi.it
Correspondence: Doriana Fruci, Bambino Gesù Children's Hospital, IRCCS, 00146 Rome, Italy.
E-mail: doriana.fruci@opbg.net
Correspondence: Lucia Di Marcotullio, Department of Molecular Medicine, Sapienza University of Rome, 00161 Rome, Italy.
E-mail: lucia.dimarcotullio@uniroma1.it

discovering new mechanisms to regulate Gli activity.[16,17] Recently, we identified endoplasmic reticulum aminopeptidase 1 (ERAP1), a key component of the antigen processing and presentation (APP) pathway able to reprogram tumor immunogenicity,[18–20] as a positive regulator of the HH pathway involved in Gli protein stability and HH-MB development.[21] We found that ERAP1 forms a complex with the deubiquitylating enzyme USP47, which promotes βTrCP degradation and Gli protein stabilization, thereby favoring cell proliferation and tumorigenesis.[21] ERAP1 inhibition reduced tumor growth in preclinical models of HH-MB,[21] suggesting that its blockade may offer an innovative approach to the treatment of HH-dependent tumors. Modulation of ERAP1 also alters peptide presentation, helping tumors to evade immune surveillance and promote an immunosuppressive environment.[22,23] Targeting ERAP1 may thus provide a dual therapeutic advantage in HH-MB, both by inactivating HH/GLI signaling and by increasing the presentation of more immunogenic peptides that enhance cytotoxic T cell responses.[24] Researchers are focusing on the development of specific and potent ERAP1 inhibitors to enhance immune responses while minimizing side effects and overcoming drug resistance. ERAP1 inhibitors could be critical in targeting HH-MB and improving clinical outcomes, but currently, there are few specific compounds for use in the clinic.[25] In this study, we identify canthin-6-one, an alkaloid naturally extracted from *Pentaceras australis* (Rutaceae),[26] hereafter referred to as N1, as a novel small molecule that binds and inhibits ERAP1 functions. We find that N1 impairs ERAP1 association with USP47 and promotes βTrCP protein stability and degradation of Gli activating factors, thereby suppressing HH-MB growth both *in vitro* and *in vivo*.

RESULTS

Virtual library and functional screening of potential ERAP1 small-molecule inhibitors

To identify new putative ERAP1 inhibitors, we used the crystallographic structure of ERAP1 in complex with the aminopeptidase inhibitor bestatin as a rigid receptor in molecular docking simulations.[27] We virtually screened an in-house library of approximately 1,000 natural products and their derivatives against the catalytic site of ERAP1.[28] Eleven compounds (N1–N11) endowed with a remarkable chemical diversity among one another, emerged as putative ligands of ERAP1 (Figure 1).[29–42] A significant proportion of these small molecules belongs to the chemical class of phenolic compounds (N2–3 and N5–9). Another compound identified was a pentacyclic triterpenoid (N4), while three other candidates belong to the chemical class of alkaloids. Alkaloids are one of the largest and most intriguing families of natural compounds, characterized by a wide structural diversity with no agreed-upon classification. They include a β-carboline alkaloid (N1), an oxazole alkaloid (N10), and an imidazole-type alkaloid (N11). To test the ability of the selected compounds to inhibit ERAP1 and affect the APP pathway, we used a cell-based ERAP1 antigen presentation assay based on the recognition of the SIINFEKL (S8L) epitope by the 25.D1.16 antibody when presented by murine H-2K^b. HeLa cells stably overexpressing the H-2K^b allele (HeLa-K^b) were transfected with a vector encoding the LEQLESIINFEKL (L13L) peptide, which requires the enzymatic activity of ERAP1 to generate the S8L epitope.[43,44] In the absence of an inhibitor, L13L-expressing HeLa-K^b cells show high levels of H-2K^b/S8L complex presentation on the cell surface, as determined by flow cytometry. Leucinethiol (LeuSH), a leucine aminopeptidase inhibitor, was included as a positive control.[45,46] All compounds were tested except N6, which was incompatible with the assay due to its yellow color. Four (N1, N3, N7, and N10) of the 10 compounds tested showed a significant dose-dependent reduction in the presentation of the H-2K^b/S8L complex on the cell surface (Figure 2A). The remaining compounds did not affect the presentation of the H-2K^b/S8L complex, even at the highest concentrations (Figure S1A). With the exception of compound N10, no effect on cell viability was observed for compounds N1, N3, and N7 at concentrations up to 10 μM (Figure S1B). We decided to focus on compound N1, the canthin-6-one, a β-carboline alkaloid with an additional D ring belonging to the canthinone alkaloid family,[32] because it is the most active in inhibiting ERAP1 compared to N3 and N7 (Figure 2A). Consistently, molecular docking simulation revealed that N1 fits into the catalytic site of ERAP1 showing good overlap with crystallographic Zn-binding inhibitors (Figure 2B). To further assess potential binding modes, additional docking simulations were performed across the entire accessible surface of ERAP1. These analyses indicated that, in addition to the catalytic site, N1 can also bind to the allosteric regulatory site near Lys685, displaying substantial overlap with the crystallographic pose of recently characterized cyclohexyl acid ERAP1 inhibitors (Figure S2).[47]

ERAP1 directly interacts with N1

To investigate the direct binding of N1 to ERAP1 in cells, we performed a cellular thermal shift assay (CETSA), a label-free method that allows the assessment and quantification of the strength with which a molecule can bind its target protein.[48] We observed that N1, but neither N3 nor N7, induced a thermal stabilization of ERAP1 (Figures 2C and S3) following the formation of new bonds between the compound and its target, shifting its melting curve forward from 48°C to 58.8°C ($\Delta T_m = 10.8°C$; Figure 2D). This evidence was further confirmed by an isothermal dose-response fingerprint (ITDRF) assay in which incubation of mouse embryonic fibroblast (MEF) lysate with increasing amounts of N1 heated to 62°C induced dose-dependent thermal stability, fixing its OC_{50} (observed concentration 50) at 0.6 μM (Figure 2E). These results demonstrate that N1 binds ERAP1 in the intact cell environment.

N1 impairs HH pathway activity

Given the role of ERAP1 as an activator of the HH pathway,[49,50] we next investigated whether N1 impairs HH activity. To this end, we performed a functional transcriptional assay in which NIH 3T3 SHH-Light II cells, stably carrying a Gli-responsive firefly luciferase reporter (Gli-RE), were treated with SAG,[49,50] a well-known synthetic agonist of SMO, alone or in combination with compound N1. We found that the luciferase activity of the HH pathway reporter was suppressed in the presence of N1 in a dose-response manner (Figure 3A) and at a much lower concentration (half-maximal

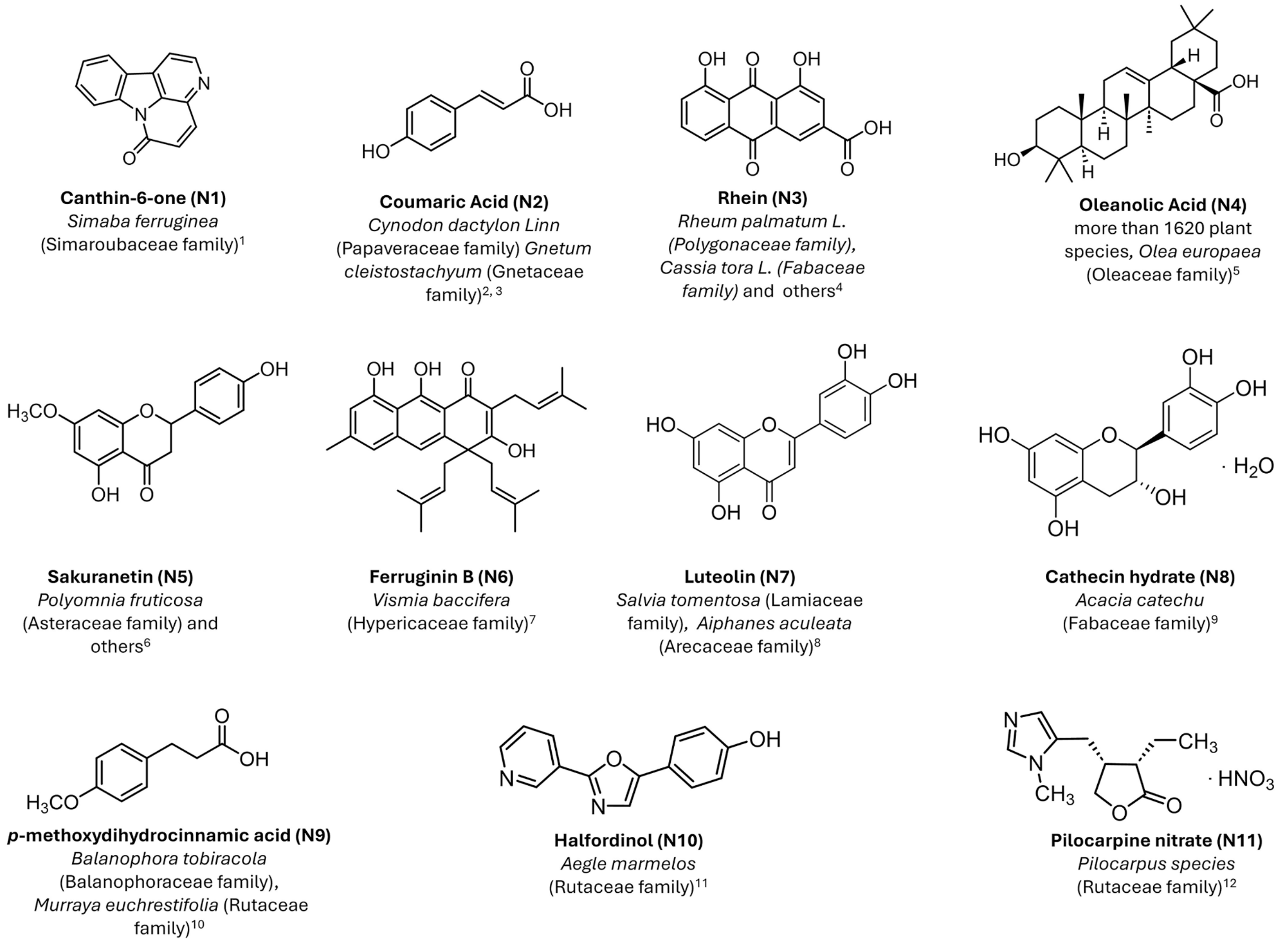

Canthin-6-one (N1)
Simaba ferruginea
(Simaroubaceae family)[1]

Coumaric Acid (N2)
Cynodon dactylon Linn
(Papaveraceae family) *Gnetum cleistostachyum* (Gnetaceae family)[2, 3]

Rhein (N3)
Rheum palmatum L. (Polygonaceae family), Cassia tora L. (Fabaceae family) and others[4]

Oleanolic Acid (N4)
more than 1620 plant species, *Olea europaea*
(Oleaceae family)[5]

Sakuranetin (N5)
Polyomnia fruticosa
(Asteraceae family) and others[6]

Ferruginin B (N6)
Vismia baccifera
(Hypericaceae family)[7]

Luteolin (N7)
Salvia tomentosa (Lamiaceae family), *Aiphanes aculeata*
(Arecaceae family)[8]

Cathecin hydrate (N8)
Acacia catechu
(Fabaceae family)[9]

***p*-methoxydihydrocinnamic acid (N9)**
Balanophora tobiracola
(Balanophoraceae family), *Murraya euchrestifolia* (Rutaceae family)[10]

Halfordinol (N10)
Aegle marmelos
(Rutaceae family)[11]

Pilocarpine nitrate (N11)
Pilocarpus species
(Rutaceae family)[12]

Figure 1. Chemical structures of the 11 natural products (N1–N11) that are identified as a putative ERAP1 ligand

The compounds include canthin-6-one (N1), coumaric acid (N2), rhein (N3), oleanolic acid (N4), sakuranetin (N5), ferruginin B (N6), luteolin (N7), cathecin hydrate (N8), *p*-methoxydihydrocinnamic acid (N9), halfordinol (N10), and pilocarpine nitrate (N11). The main plant sources and their respective taxonomic families are reported next to each compound.

inhibitory concentration [IC_{50}] = 46.24 nM) than LeuSH (IC_{50} = 629.1 nM) (Figure 3B). Consistent with the above data, N3 and N7 were unable to inhibit HH pathway activity (Figure S4). Importantly, N1 did not affect luciferase activity driven by either the HH-related or HH-unrelated signaling pathway (i.e., Wnt/β-catenin and Jun/AP1, respectively), demonstrating the specificity of action for HH signaling (Figure S5).

The inhibitory properties of N1 on the HH pathway were also confirmed in *Ptch1*$^{-/-}$ MEFs, in which the pathway is constitutively active due to the loss of the *Ptch1* repressor gene. In these cells, N1 significantly reduced the mRNA and protein levels of endogenous *Gli1*, the final and most potent effector of the HH pathway (Figures 3C–3E),[51] as well as the mRNA expression of the other HH target genes, *Gli2* and *CycD2* (Figure 3C). The observed effect is stronger than that obtained with LeuSH at the highest concentrations (Figures 3C–3E).

To investigate whether the effect of N1 on HH pathway inhibition is independent of ERAP1, we genetically silenced ERAP1 in *Ptch1*$^{-/-}$ MEFs by infection with lentiviral particles encoding small hairpin ERAP1 (shERAP1) or shCTR (short hairpin control). Treatment with N1 was ineffective in ERAP1 knockdown cells. Indeed, the reduction of HH target genes at the protein and/or mRNA level in these cells was exclusively due to the genetic silencing of ERAP1 and not to a dose-response effect of the inhibitor as in control cells (Figures 3F–3H). As expected, the expression of ectopic ERAP1 in *Ptch1*$^{-/-}$ ERAP1 knockdown MEFs rendered the cells sensitive to N1 again, as shown by the significant decrease in both Gli1 mRNA and protein levels (Figure 3I). Finally, to further verify the N1 specificity for ERAP1, *Ptch1*$^{-/-}$ MEFs genetically silenced for *ERAP1* were transfected with a plasmid encoding the wild-type form of Gli1 (HA-WT Gli1). Remarkably, treatment with increasing concentrations of N1 did not alter Gli1 mRNA or protein levels (Figure 3J). These results confirm that the inhibitory effect of N1 on the HH

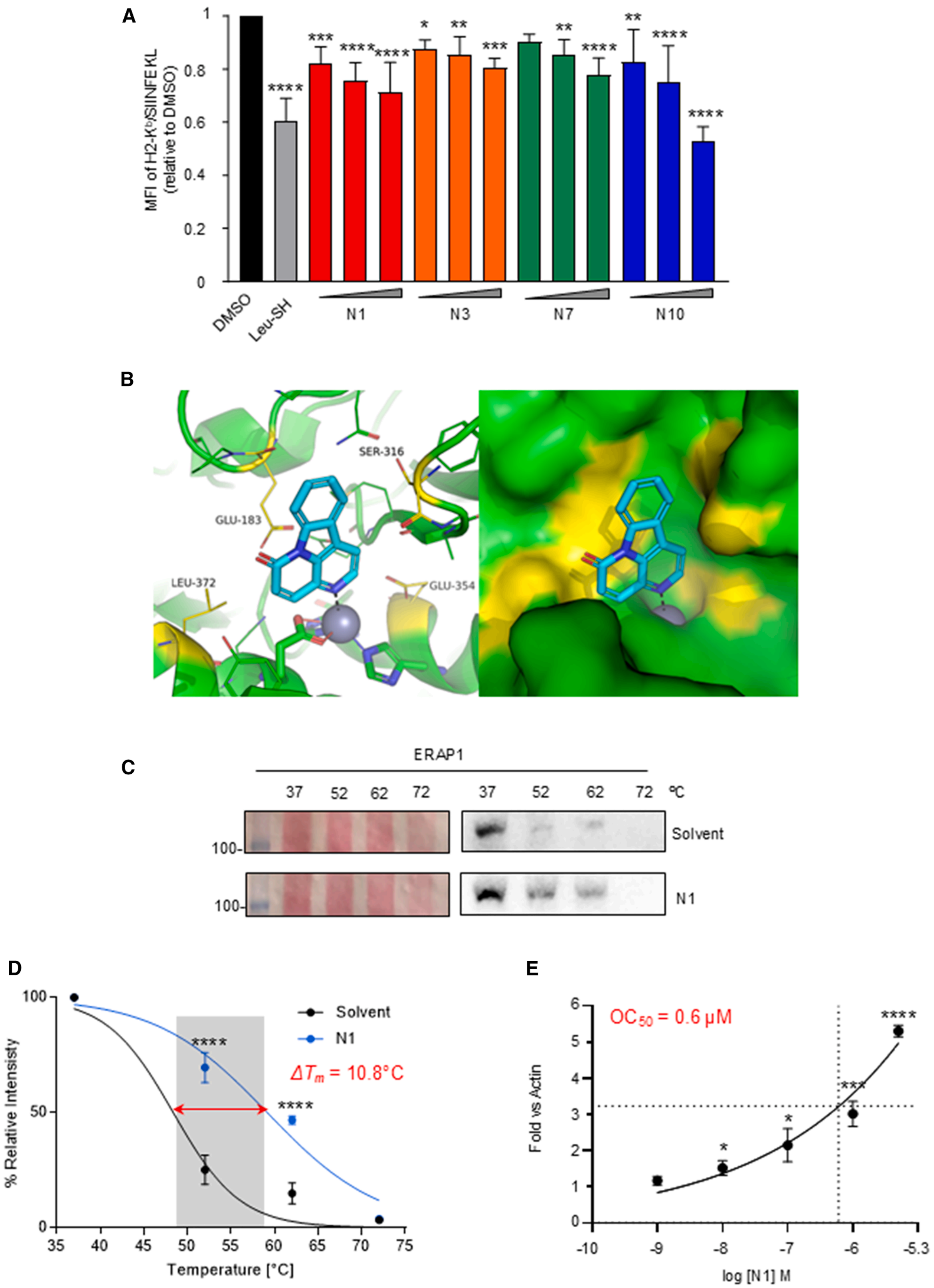

(legend on next page)

pathway is mediated by ERAP1 and that this compound specifically targets ERAP1.

N1 inhibits the ERAP1/USP47 interaction by increasing the stability of βTrCP

To elucidate the molecular mechanism by which pharmacological N1-dependent ERAP1 inhibition affects HH pathway activity, we first evaluated the effect of N1 in MEFs in which the HH pathway is activated by SAG treatment. Interestingly, we observed a significant increase in the protein levels of βTrCP and Gli3R and a concomitant decrease in Gli1 and Gli2 (Figures 4A and 4B). Accordingly, treatment with increasing amounts of N1 leads to a reduction of HH signature genes at the mRNA level (Figure 4C). Interestingly, the *in vitro* pull-down assay demonstrated that N1, by binding to ERAP1, is able to displace the direct interaction of ERAP1 with USP47 (Figures 4D and 4E). These data were also confirmed by the co-immunoprecipitation experiment, which showed that treatment with increasing concentrations of N1 inhibited the ERAP1/USP47 interaction in a dose-dependent manner (Figures 4F and 4G). In addition, the proximity ligation assay (PLA) revealed that N1 robustly decreased the interaction between ERAP1 and USP47, as indicated by the decreased number of red dots (Figures 4H and 4I). Displacement of USP47 from ERAP1 by N1 resulted in a dose-dependent increase in USP47 association with βTrCP (Figures 4J and 4K). Consistent with our previous findings that USP47 overexpression stabilizes βTrCP and promotes Gli1 degradation,[21] treatment with N1 under USP47 overexpression further enhances this effect (Figures S6A–S6C). Moreover, N1 treatment alone increased the half-life of βTrCP (Figures 4L and 4M), an effect attributable to reduced polyubiquitylation, as assessed by the *in vivo* ubiquitylation assay (Figure S6D). Overall, these data indicate that N1 disrupts the ERAP1-dependent regulation of the HH pathway, thereby altering its activity.

SAXS analysis confirms a conformational change

ERAP1 has been crystallized in two different conformations: open and closed.[52,53] While ERAP1 typically maintains an open conformation in solution, some inhibitors promote and stabilize its closed conformation.[52,53] We hypothesized that the binding of N1 to ERAP1 might induce a conformational change of this enzyme, preventing it from binding to USP47 and thus interfering with the activation of the HH pathway by ERAP1. To verify this hypothesis, we studied the tertiary structure of recombinant ERAP1 in solution with and without N1 using small-angle X-ray scattering (SAXS) analysis. We obtained recombinant WT ERAP1 expressed in baculovirus-infected Hi5 insect cells and purified them to homogeneity. The purified sample was highly pure, homogenous, and folded, as demonstrated by SDS-PAGE, mass photometry (MP), and TSA analysis (Figure S7). As expected, SAXS analysis of ERAP1 and the ERAP1/N1 complex at 300 μM revealed an important change in the tertiary structure of ERAP1. As shown in Figures 4N (green shape) and S8A–S8C, the ATSAS software showed good agreement, with a χ^2 of 0.996, between the ERAP1 sample and the SAXS experimental data, with a good radius of gyration value. In the case of the ERAP1/N1 complex, we also obtained a reasonable agreement with a χ^2 of 1.165, and it is possible to appreciate the different tertiary organization of the protein/inhibitor complex (Figure 4N, yellow shape). The comparison between the two shapes of our samples clearly shows that the binding of N1 to the ERAP1 protein induces a conformational change in which the structure of the complex adopts a more elongated conformation (Figure 4N). This change would result in the protein having different exposed contact surfaces compared to the structure without N1, which adopts a more globular shape, preventing binding with USP47. Based on our experimental data, we propose a model of ERAP1 conformational change. As shown in Figures S8D and S8E, our model incorporates all four ERAP1 domains and suggests that the inhibitor may induce an approximately 90° rotation of the N-terminal domain (shown in red) away from the two central domains (shown in blue and orange). This movement would result in an opening of the ERAP1 structure, thereby exposing regions of the protein that could engage in interactions with other cellular partners.

N1 impairs HH-dependent growth of cerebellar GNPs

The HH signaling pathway is crucial for cerebellum development as it controls the expansion of GNPs under HH stimuli released by Purkinje cells. In mice, physiological disruption of the HH signal after the first postnatal week results in the arrest of GNP growth and induction of their differentiation into mature granules.[54] Genetic or epigenetic alterations in key components of the HH pathway can lead to failure of signal withdrawal, stimulating uncontrolled proliferation of GNPs and promoting their tumorigenic transformation.[55,56]

Figure 2. Functional screening of selected compounds and docking-based binding pose of compound N1 confirmed by ERAP1 thermal stabilization

(A) Relative expression of H-2K^b/SIINFEKL (S8L) complex in HeLa-K^b cells transfected with LEQLESIINFEKL (L13L) and treated with increasing concentrations (5, 10, and 30 μM) of the indicated compounds and analyzed by flow cytometry. Leu-SH-treated cells were used as positive controls. Results of samples tested in triplicate in at least three independent assays are shown. Statistical significance was assessed using one-way ANOVA (F(13, 55) = 19.23; $p < 0.0001$). (B) Putative binding mode of N1 within the catalytic site of the ERAP1 crystallographic structure as predicted by molecular docking simulations. The ERAP1 inhibitor is shown as cyan sticks, and Zn coordination is highlighted by a black dashed line. The catalytic Zn(II) ion is shown as a gray sphere; residues within 5 Å from N1 are shown as lines, while residues surrounding the small molecules are colored yellow and labeled. Zn-binding residues are shown as green sticks. Left: illustration and line representation of the ERAP1 catalytic site. Right: surface representation of the ERAP1 catalytic site. (C) N1-mediated stabilization of ERAP1 protein. Representative western blot showing thermostable ERAP1 after indicated heat shocks following treatment with N1 or DMSO. Red Ponceau (RP) staining was used as a loading control. (D) Quantification of thermostable ERAP1 from three independent experiments. The stabilization of ERAP1 in the presence of N1 is expressed as the mean (SD) of ΔT_m. Statistical analyses were performed using two-way ANOVA: treatment F (1, 4) = 130.3, $p = 0.0003$; temperature F(3, 12) = 787.7, $p < 0.0001$; and interaction F(3, 12) = 60.42, $p < 0.0001$. (E) Quantification of the dose response of thermostable ERAP1 by N1 at 62°C; $OC_{50} = 0.6$ μM, at which 50% of ERAP1 is occupied by N1 in cells. Significant differences vs. CTR are indicated as $^{*}p < 0.05$; $^{**}p < 0.01$; $^{***}p < 0.001$; $^{****}p < 0.0001$.

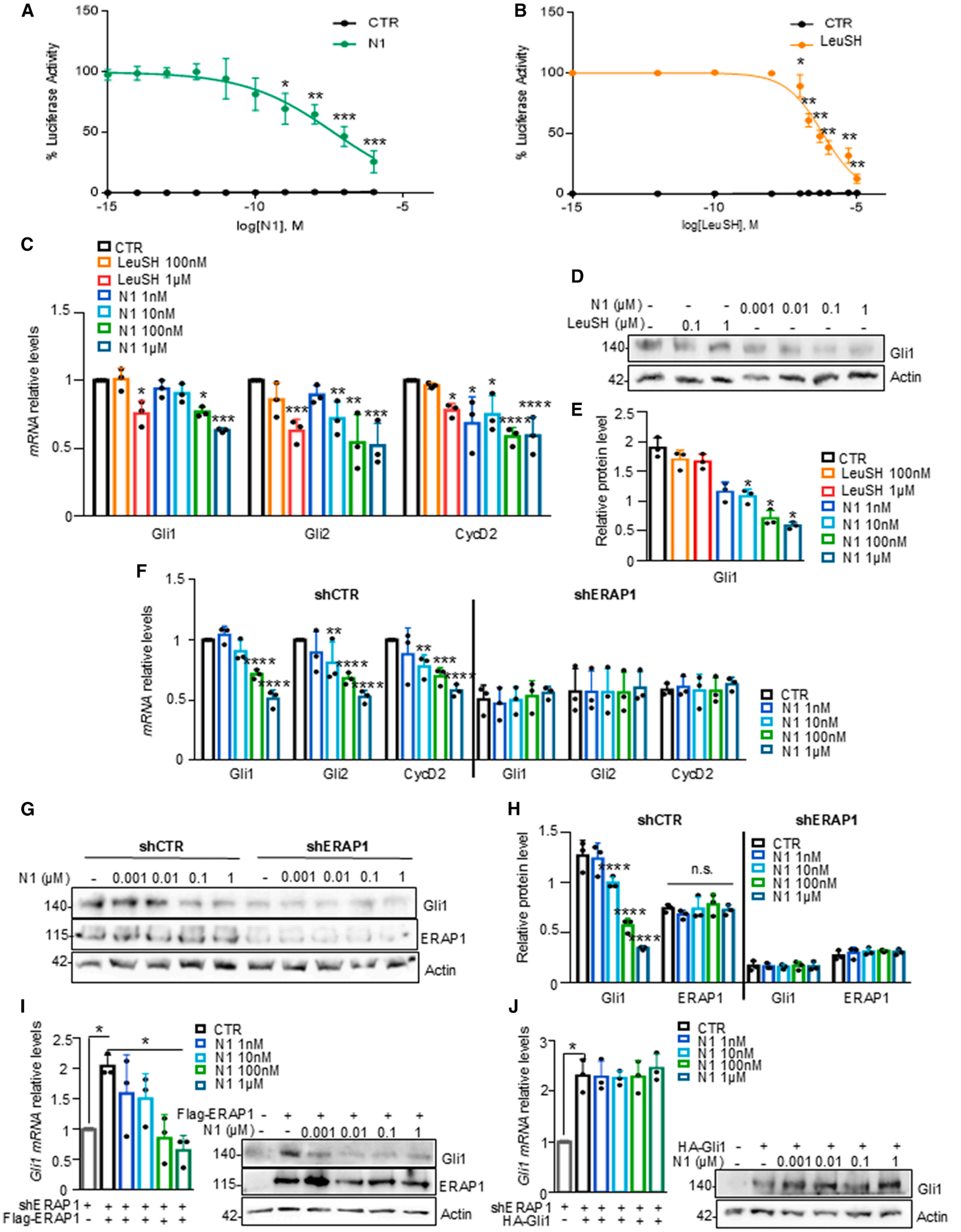

(legend on next page)

To assess whether N1 could interfere with GNP growth events, we first evaluated its ability to suppress HH-dependent proliferation of 5-day-old mouse GNPs. As shown in Figures 5A and 5B, N1 downregulated SAG-enhanced 5-ethynyl-2′-deoxyuridine (EdU) uptake by GNPs in a dose-dependent manner. Accordingly, reduced expression levels of HH signature genes and cell growth-related genes were observed in N1-treated GNPs (Figures 5C–5E), confirming that the effect of this compound on GNP proliferation is related to the impairment of HH signaling activity.

Consistent with previous findings, we confirmed that the presence of ERAP1 is required for the function of N1. Indeed, we observed that N1 is unable to further reduce the expression of the HH signature and cell-cycle-related genes at mRNA and/or protein levels in GNPs derived from constitutionally ERAP1 knockout (ERAP KO) mice,[44,57] compared to GNPs from ERAP1 WT mice (Figures 5F–5H).

N1 inhibits HH-MB cell growth *in vitro*

Since GNPs are considered the cells of origin of HH-MB,[1,58] the most common and aggressive pediatric brain malignancy,[59] we next evaluated the effect of N1 on HH-MB growth. Treatment with N1 significantly reduced the proliferation of Med1 cells, an HH-MB cell line,[60,61] in a dose- and time-dependent manner (Figure S9A), and induced apoptosis, as shown by increased caspase-3/-7 compared to controls (Figures S9B, S9C, S9E, and S9F). Consistently, expression of HH signature genes was decreased at both mRNA and protein levels in Med1 cells (Figures S9D–S9F). Similar results were obtained in the murine basal cell carcinoma (BCC) cell line ASZ001 (Figure S10), a well-characterized HH-dependent tumor model,[62,63] further confirming the efficacy of N1 in suppressing aberrant HH pathway activation in multiple contexts.

To validate these findings, short-term cultures of primary HH-MB cells isolated from tumors of *Math1-Cre/Ptch1*$^{C/C}$ mice, a widely used HH-dependent tumorigenesis model,[51,64,65] were treated with increasing concentrations of N1. As expected, N1 strongly reduced the proliferation of primary HH-MB cells in a dose- and time-dependent manner (Figure 6A) and reduced bromodeoxyuridine (BrdU) uptake (Figures 6B and 6C). In line with results in Med1 cells, N1 treatment induced apoptosis in primary HH-MB cells, as shown by increased annexin V staining and caspase-3/-7 activity (Figures 6D–6F). Moreover, N1 downregulated HH target genes and proliferation markers at the mRNA level (Figure 6G) and decreased Gli1 and Gli2 protein expression, while it increased βTrCP, Gli3R, and the pro-apoptotic markers cleaved poly (ADP-ribose) polymerase (PARP) and cleaved caspase-3 (Figures 6H and 6I).

To further validate the specificity of N1 for ERAP1, primary HH-MB cells from *Math1-Cre/Ptch1*$^{C/C}$ mice were genetically silenced for ERAP1 and treated with N1. As shown in Figure 6G, the downregulation of the HH signature upon genetic silencing of ERAP1 is attributable only to the absence of ERAP1, with no additional effect due to N1 treatment (Figure 6J).

Aberrant activation of the HH pathway controls several aspects of tumorigenesis, including the generation and maintenance of a subpopulation of tumor cells that exhibit the cancer stem cell phenotype. MB-stem-like cells (SLCs) exhibit self-renewal and tumor-initiating properties and are able to differentiate into transient amplifying cells that contribute to tumor cell heterogeneity.[66–68] These cells are involved in tumor maintenance, metastasis, and relapse and are a major cause of chemoresistance. They are therefore considered an interesting druggable target to test the therapeutic potential of N1 for the treatment of HH-MB.[66,69]

To obtain MB-SLCs, tumor cells isolated from MB of *Math1-Cre/Ptch1*$^{C/C}$ mice were cultured as neurospheres in a culture medium without epidermal growth factor (EGF) and β fibroblast growth factor (βFGF) to maintain the characteristics of HH-subtype MB *in vivo* and avoid differentiation of GNPs. Interestingly, pharmacological inhibition of ERAP1 by N1 decreased the neurosphere-forming ability of MB-SLCs (Figures S11A and S11B), and a reduction in the number and size of these cells was observed (Figures S11C and S11D). Accordingly, MB-SLCs neurospheres treated with increasing amounts of N1 showed altered HH-pathway activity, as evaluated by the significant reduction in mRNA and/or protein expression of HH-pathway target genes, as well as genes related to stemness, growth, and oncogenicity (Figures S11E–S11G). Furthermore,

Figure 3. Effect of N1 on HH pathway activity

(A and B) Dose-response curve of compound N1 (A) and LeuSH (B) in SAG-treated NIH 3T3 SHH-Light II cells. Treatment time was 48 h and data were normalized against Renilla luciferase. (C–E) mRNA expression levels (C) and protein expression levels (D) of HH target genes of *Ptch1*$^{-/-}$ MEFs treated for 48 h, with the indicated concentrations of N1 or DMSO as negative control and LeuSH as positive control. Densitometric analysis of Gli1 protein shown in (D). (F–H) *Ptch1*$^{-/-}$ MEFs were transduced with shCTR or shERAP1 constructs and treated with N1 at the indicated concentrations. (F) Quantitative real-time PCR analysis of endogenous HH target genes and proliferation-related genes. (G and H) Representative immunoblotting analysis (G) and densitometric analysis (H) of endogenous HH target genes. mRNA levels were normalized to endogenous control *HPRT*. All data are the mean of three independent experiments. (I) Gli1 mRNA and protein levels in *Ptch1*$^{-/-}$ MEFs genetically silenced for *ERAP1* upon ectopic expression of FLAG-ERAP1 treated with N1 at the indicated concentration for 48 h. (J) Gli1 mRNA and protein levels in *Ptch1*$^{-/-}$ MEFs genetically silenced for *ERAP1* following ectopic expression of HA-Gli1 and treated with increasing amounts of N1. Data are presented as mean (SD) from at least three independent experiments. Statistical analyses were performed as follows: (A and B) two-sided Student's *t* test; (C) two-way ANOVA, treatment F(6, 36) = 22.10, $p < 0.0001$; gene F(2, 6) = 5.35, $p = 0.0464$; interaction F(6, 36) = 1.634, $p = 0.1662$; (E) one-way ANOVA, F(1.355, 2.709) = 48.50, $p = 0.0080$; (F) two-way ANOVA, treatment F(4, 48) = 27.08, $p < 0.0001$; protein F(5, 12) = 5.59, $p = 0.0069$; interaction F(20, 48) = 8.61, $p < 0.0001$; (H) two-way ANOVA, treatment F(4, 32) = 29.81, $p < 0.0001$; protein F(4, 32) = 29.81, $p < 0.0001$; interaction F (12, 32) = 35.70, $p < 0.0001$; (I) one-way ANOVA, F(1.202, 2.404) = 14.86, $p = 0.0450$; and (J) one-way ANOVA, F(1.694, 3.388) = 11.36, $p = 0.0325$. Statistical significance vs. CTR is indicated as $^{*}p < 0.05$; $^{**}p < 0.01$; $^{***}p < 0.001$; $^{****}p < 0.0001$.

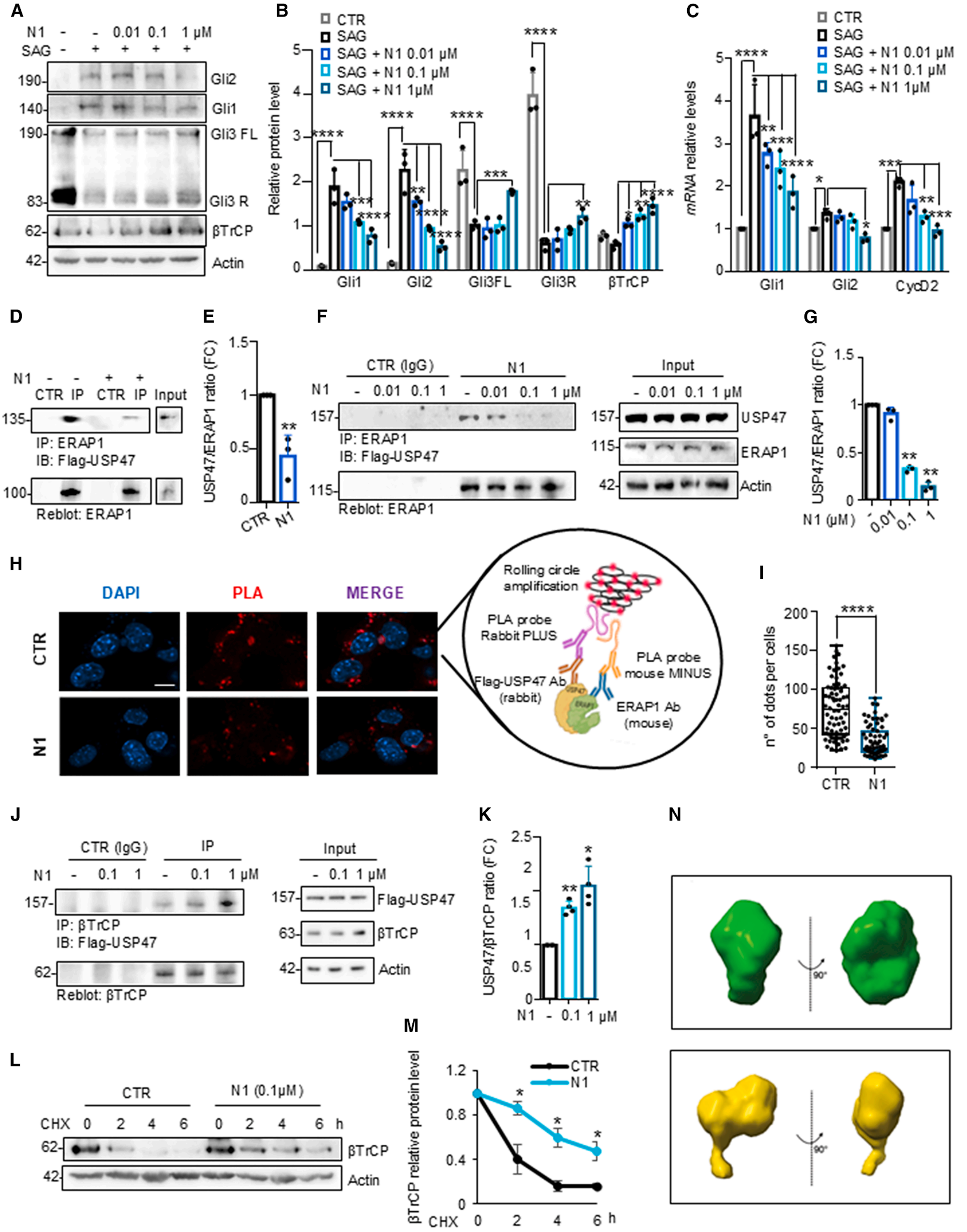

(legend on next page)

inhibition of ERAP1 by N1 in these cells promotes an increase in Gli3R, with a marked reduction in Gli1 and Gli2 protein levels (Figures S11F and S11G).

N1 inhibits HH-MB tumor growth *in vivo*

Based on the *in vitro* data, we investigated the ability of N1 to block HH-MB tumor growth *in vivo*. To this purpose, immunocompromised mice were subcutaneously (s.c.) engrafted with Med1 cells, and the resulting tumor masses were treated every other day with intratumoral injections of N1 at a concentration of 1 mg/kg or vehicle. In agreement with the *in vitro* data, we observed a reduction in the growth of tumor masses treated with N1 compared to controls (Figures S9H and S9I), with a concomitant decrease in the expression of endogenous HH target genes at the mRNA level (Figure S9J).

The *in vivo* anti-tumor effect of N1 on HH-MB was also confirmed in another heterotopic allograft model in which NOD/SCID gamma (NSG) mice were engrafted with spontaneous primary MB from *Math1-Cre/Ptch1*$^{C/C}$ mice, and the resulting tumor masses were treated with N1 or vehicle. Notably, we observed a significant reduction in tumor growth in N1-treated masses compared to the control group (Figures S12A and S12B). Immunohistochemical (IHC) staining showed reduced cellularity and decreased expression of the proliferation marker Ki67 in the tumor cells, while NeuN and cleaved caspase-3 expression was increased (Figures S12C–S12F). Accordingly, the expression of the HH signature, proliferation, neural differentiation-related genes, and the apoptotic marker cleaved caspase-3 was reduced at both mRNA and/or protein levels in N1-treated tumor masses compared to controls (Figures S12G and S12I), confirming that this compound impairs tumor growth by counteracting the activity of the HH pathway also in an *in vivo* context.

To investigate whether N1 is able to cross the blood-brain barrier (BBB), WT CD1 mice were treated with N1 intravenously (i.v.; 1 mg/kg) using β-cyclodextrins as vehicle at five different time points (0.5, 1, 2, 4, and 6 h), and the concentration of N1 in brain and cerebellum extracts was analyzed by ultra-high-performance liquid chromatography coupled to electrospray tandem mass spectrometry (UHPLC-MS/MS). The quantitative analysis of N1 in cerebellum and brain tissues was expressed as nanograms of N1 per gram of brain or cerebellum (Figure 7A; Figure S13; Table S1).

Based on the UHPLC-MS/MS results, we performed an orthotopic allograft model in which NSG mice were engrafted with spontaneous primary MB cells from *Math1-Cre/Ptch1*$^{C/C}$ mice. Ten days after tumor implantation, mice were treated i.v. with N1 (1 mg/kg) or vehicle twice weekly for 25 days. Consistent with the previous data, we observed a significant reduction in HH-MB tumor growth in N1-treated mice compared to control mice (Figures 7B and 7C), which correlates with reduced Ki67 expression and increased NeuN expression and cleaved caspase-3 in tumor cells (Figures 7B and 7D–7F). To further evaluate the effect of ERAP1 inhibition by N1 in a natural tumor niche for HH-MB growth, symptomatic *Gfap-Cre/Ptch1*$^{C/C}$ mice were treated with N1 or vehicle. As expected, N1 treatment reduced the expression of the HH pathway target genes at both mRNA and protein levels and increased the protein level of βTrCP (Figure S14). Interestingly, we found that i.v. treatment with N1 significantly improved survival in *Math1-Cre/Ptch1*$^{C/C}$ mice (Figure 7G). In conclusion, our findings indicate that ERAP1 inhibition by N1 strongly inhibits HH-MB tumor growth and promotes cell differentiation.

N1 impairs growth of human SHH-MB PDX cells

Finally, we investigated the effect of ERAP1 inhibition by N1 in human SHH-MB patient-derived xenograft (PDX).[70] Similar to murine tumor models, treatment with N1 reduced cellular confluence in SHH-MB PDX cells in a dose- and time-dependent manner (Figure 8A), accompanied by the decreased expression of HH target genes at both mRNA and protein levels (Figures 8B and 8C). In accordance with the data obtained in HH-dependent models, N1 treatment promoted apoptotic cell death also in SHH-MB PDX cells,

Figure 4. N1 impairs ERAP1/USP47 interaction and promotes βTrCP stability

(A–C) Representative immunoblotting analysis of the indicated proteins (A and B) and quantitative real-time PCR (C) of HH target genes in SAG-treated MEF WT in combination with different amounts of N1 or DMSO as control for 48 h. (B) Densitometric analysis of the proteins shown in (A). (D) *In vitro* pull-down assay showing the direct interaction between ERAP1 and FLAG-USP47. (E) Densitometric analysis of the experiment shown in (D). (F) MEFs were transfected with FLAG-USP47 and treated with increasing amounts of N1 for 48 h. The interaction between FLAG-USP47 and endogenous ERAP1 was assessed by immunoprecipitation and immunoblotting with the indicated antibodies. (G) Densitometric analysis of the binding affinity between FLAG-USP47 and ERAP1 after N1 treatment. (H) Representative image of the interaction between ERAP1 and FLAG-USP47 by the proximity ligation assay (PLA) with or without N1 treatment (1 μM). After cell fixation, PLA was performed with antibodies against ERAP1 (1:50) and FLAG-USP47 (1:500). The detected interaction is indicated by red dots. Nuclei were counterstained with DAPI (blue). Scale bar: 10 μM. The schematic diagram of the PLA method used in this study is shown on the right. (I) Number of interactions (dots per nucleus) detected in (H). (J) MEFs were transfected with FLAG-USP47 and treated with N1 at the indicated concentration for 48 h. The interaction between FLAG-USP47 and endogenous βTrCP was detected as described in (F). (K) Densitometric analysis of the binding affinity of FLAG-USP47 and (J). (L) βTrCP protein levels in WT MEFs treated with N1 or DMSO as control and treated with CHX (100 μg/mL) at different time points after 24 h. (M) Densitometric analysis of actin-normalized βTrCP levels of the experiment shown in (L). (N) (Top) The ERAP1 shape model after SAXS data refinement in ChimeraX; (bottom) the shape model of the ERAP1/N1 complex obtained through the same procedure. This model provides a speculative interpretation of the open conformation of ERAP1 upon N1 binding, based on domain modeling in ChimeraX, in the absence of high-resolution structural data for the inhibitor-bound state. For western blot analysis, actin was used as a loading control. Results are shown as mean (SD) from a minimum of three independent experiments. Statistical analyses were performed as follows: (B) two-way ANOVA, treatment F(4, 40) = 6.98, $p = 0.0002$; protein F(4, 10) = 21.42, $p < 0.0001$; interaction F(16, 40) = 51.29, $p < 0.000$; (C) two-way ANOVA, treatment F(4, 24) = 33.38, $p < 0.0001$; gene F(2, 6) = 68.21, $p < 0.0001$; interaction F(8, 24) = 6.87, $p = 0.0001$; (E) two-sided Student's *t* test; (G) one-way ANOVA, F(1.426, 2.853) = 373.5, $p = 0.0004$; (I) two-sided Student's *t* test; (K) one-way ANOVA, F(1.181, 3.543) = 30.06, $p = 0.0072$; and (L) two-sided Student's *t* test. Statistical significance vs. SAG (B and C) or CTR (E, G, I, K, and L) is indicated as $^{*}p < 0.05$; $^{**}p < 0.01$; $^{***}p < 0.001$; $^{****}p < 0.0001$.

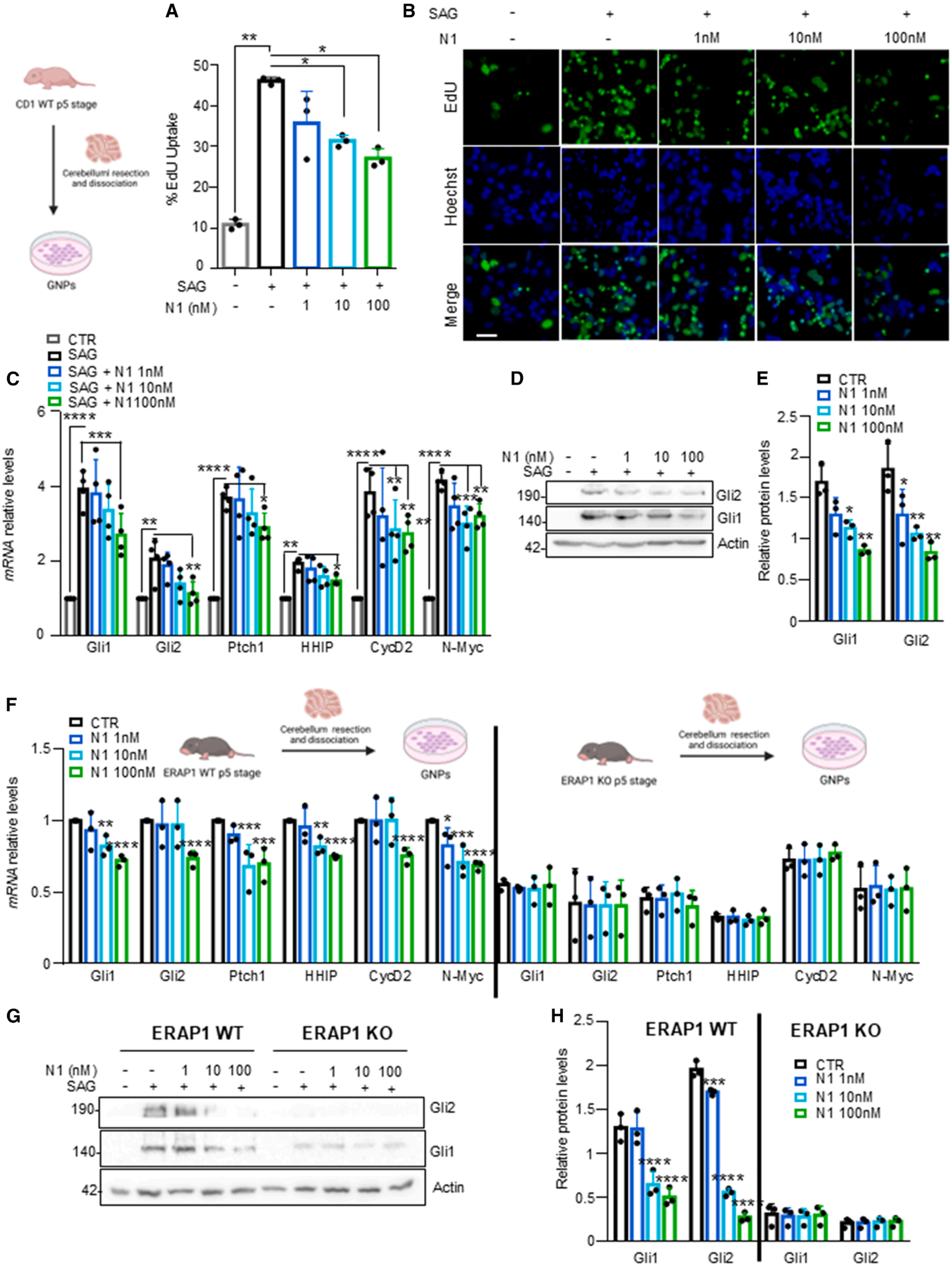

(legend on next page)

as shown by increased caspase-3/-7 activity compared to controls (Figure 8D). Notably, this effect appeared to be specific to the HH subgroup, as N1 treatment did not impair growth of HH-independent immortalized human MB cell lines (Figures S15A–S15C) or group 3 MB PDX (Figure 8E). Given that the ERAP1 regulatory network positively regulates the HH pathway, we hypothesized that its inhibition might sensitize HH-MBs to HH/SMO inhibitors. Importantly, dual treatment with N1 and the SMO inhibitor GDC-0449[71] showed synergistic effect in SHH-MB PDX cells, particularly at N1 concentrations of 5–10 μM (Figures 8F–8H). Similar results were obtained also in primary murine HH-MB cells treated with N1 in combination with SMO antagonist GDC-0449 or the GLI1 inhibitor GANT61[72] (Figure S16), suggesting that complementary mechanisms of action between upstream and downstream inhibitors may underlie the observed synergy and represent a potential therapeutic strategy.

DISCUSSION

Brain tumors are the most common solid tumors in childhood, and MB accounts for nearly 20% of all pediatric brain malignancies.[73] MB is classified as a grade IV tumor by the World Health Organization and arises from the cerebellum or posterior fossa. HH-MB, the best-understood subgroup, arises from the neoplastic transformation of GNPs.[74] The proliferation of these cells is finely orchestrated by HH signaling, and aberrant activation of this pathway has been implicated in the onset and progression of MB. Although current treatments have improved the 5-year survival rates to approximately 70%, mortality remains significant and surviving patients suffer from severe long-term side effects. Over the past two decades, HH signaling has emerged as an attractive druggable target, and several pathway-specific inhibitors have entered the clinic.[75,76] However, due to acquired drug resistance and the side effects of the current HH inhibitors, there is an urgent need to identify more effective therapies. This emphasizes the importance of unveiling the molecular mechanisms underlying the control of HH signaling for the discovery of novel druggable targets.[77] In this context, we have recently identified ERAP1 as a key player in the HH pathway and a promising therapeutic target for HH-MB.[21] ERAP1 is a well-studied aminopeptidase for its role in APP, a mechanism that leads to the production of high-affinity peptides for binding to major histocompatibility complex class I molecules.[78] Loss of ERAP1 function results in the generation of a novel immunopeptidome that stimulates anti-tumor immune responses, leading to tumor regression in several mouse tumor models.[20,45,79] These findings suggest that modulation of ERAP1 function could be a novel tool in cancer immunotherapy, highlighting the importance of identifying new selective and effective ERAP1 inhibitors.

In this study, we focused on the relevance of natural products as a useful source in cancer therapy. It is known that natural compounds account for more than one-third of all US Food and Drug Administration (FDA)-approved new molecular entities, and one-fourth of these are derived from plants.[80] Moreover, among human diseases, cancer therapy is the most important application area for natural products.[80]

For several years, great efforts have been made to identify new HH inhibitors able to suppress its aberrant activation. The first discovery was cyclopamine, an alkaloid derived from the *Liliaceae* family, which acts as a SMO antagonist and finds its application in HH-dependent tumors.[49] In addition, many other natural products have been developed to interfere with HH signaling in cancers, acting both upstream and downstream of SMO.[81,82] However, pharmacological HH inhibitors have several limitations, including poor pharmacokinetics, severe side effects, and the emergence of drug resistance due to point mutations in the molecular targets. These issues prompted us to discover new small molecules that act as HH inhibitors with low toxicity and high specificity for their targets. Here, we have identified N1 as a new inhibitor of ERAP1 that acts as an HH antagonist. N1 shows high selectivity for ERAP1 and specifically suppresses HH-MB tumor growth both *in vitro* and *in vivo*.

N1 belongs to a subclass of β-carboline alkaloids isolated from a variety of plant species. Recent studies show that this compound may have potential therapeutic effects in many oncogenic and inflammatory diseases.[83–86] For example, N1 limits tumor cell proliferation and infection by counteracting the excessive release of pro-inflammatory cytokines and mediators (e.g., interleukin [IL]-1β, IL-6, tumor necrosis factor α, nitric oxide, prostaglandin E2) in various cell types, thereby regulating the activation of several signaling cascades, such as the nuclear factor κB, and phosphatidylinositol 3-kinase-Akt pathways.[86–88] In addition, N1 and its derivatives

Figure 5. N1 inhibits HH-dependent cell growth of cerebellar granule neuron progenitors

(A) Percentage of EdU uptake in cerebellar granule neuron progenitors (GNPs) isolated from 5-day-old mice treated with DMSO (control), SAG, or SAG in combination with N1 at the indicated concentrations for 48 h. EdU incorporation was calculated to the total number of cells counted. (B) Representative images of the GNPs EdU assay shown in (A). Scale bar represents 20 μM. (C) Quantitative real-time PCR analysis shows the mRNA expression levels of HH targets and proliferation-related genes determined in GNP cultures treated with SAG alone or in combination with compound N1 for 48 h. (D) Immunoblotting analysis of protein lysate from GNPs treated with SAG alone or in combination with N1 at the indicated concentrations. (E) Densitometric analysis of protein shown in (D). (F–H) GNPs from 5-day-old ERAP1 WT mice and ERAP1 KO mice. mRNA expression levels (F) and protein expression levels (G) of endogenous HH targets and proliferation-related genes are shown. (H) Densitometric analysis of the protein shown in (G). Results in (C) and (F) were normalized to endogenous control *HPRT* and represent the mean of three independent experiments. In (D) and (G), actin was used as a loading control. Data are presented as mean (SD) from at least three independent experiments. Statistical analyses were performed using two-way ANOVA, unless otherwise specified, with treatment, gene, or protein as factors: (B) one-way ANOVA, F(1.076, 2.152) = 30.58, $p = 0.0264$; (C) treatment F(4, 72) = 107.3, $p < 0.0001$; gene F(5, 18) = 15.05, $p < 0.0001$; interaction F(20, 72) = 4.33, $p < 0.0001$; (E) treatment F(3, 12) = 18.01, $p < 0.0001$; protein F(1, 4) = 0.25, $p = 0.6413$; interaction F(3, 12) = 0.30, $p = 0.8277$; (F) treatment F(3, 72) = 36.06, $p < 0.0001$; gene F(11, 24) = 15.86, $p < 0.0001$; interaction F(33, 72) = 4.56, $p < 0.0001$; and (H) treatment F(3, 24) = 783.5, $p < 0.0001$; protein F(3, 8) = 67.80, $p < 0.0001$; interaction F(9, 24) = 323.6, $p < 0.0001$. Statistical significance vs. SAG (A and C) or CTR (E, F, and H) are indicated as $^{*}p < 0.05$; $^{**}p < 0.01$; $^{***}p < 0.001$; $^{****}p < 0.0001$.

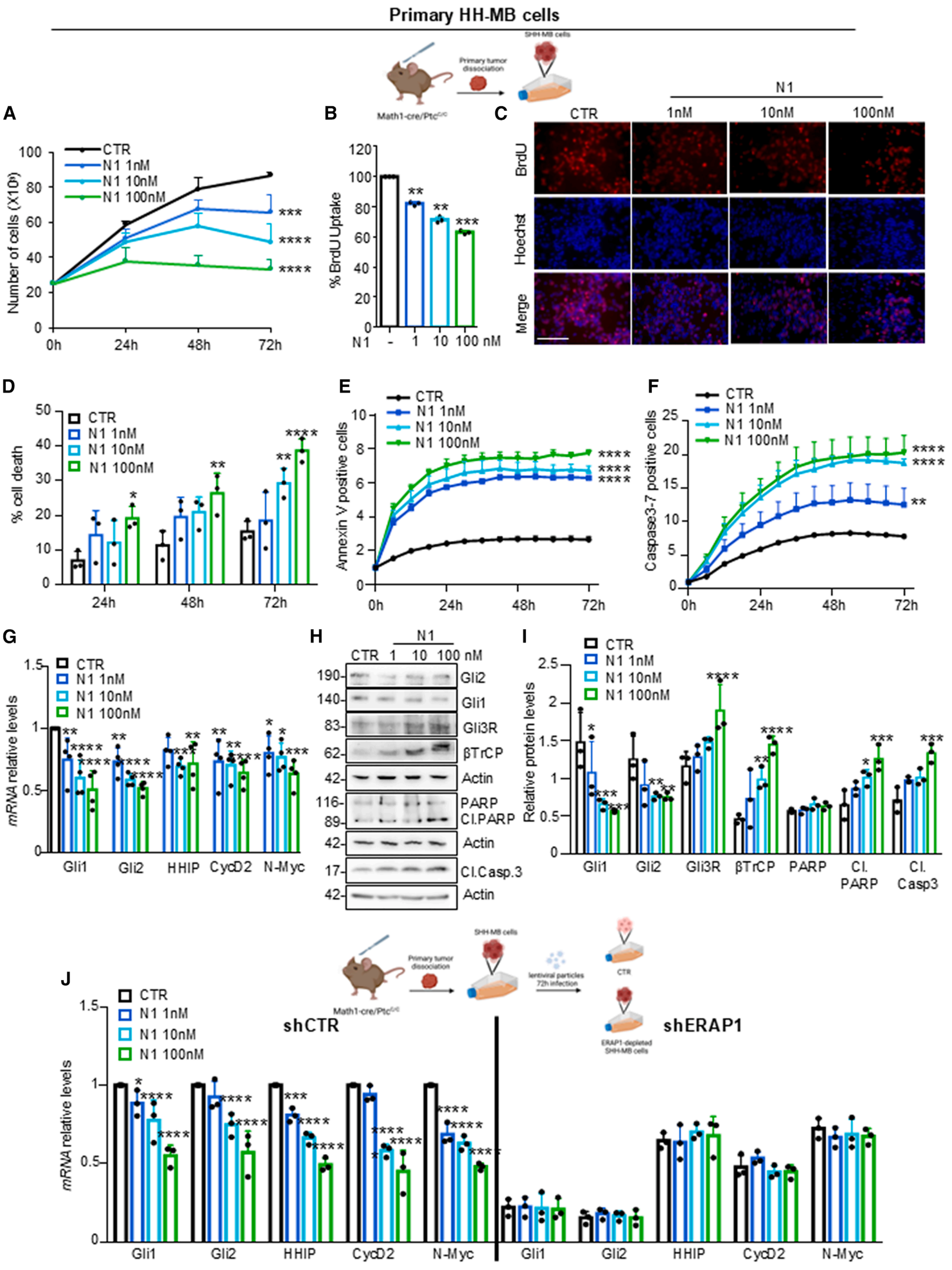

(legend on next page)

have been shown to have significant anti-proliferative effects on many tumor cell lines, demonstrating anti-tumor activity.[89,90]

Despite the potential curative properties of N1, it should not be underestimated that several studies have demonstrated the potential cytotoxicity of this compound in human lung, breast, and epithelial cancer cell lines.[87,88] In this work, we demonstrated that N1, at the highest effective dose used *in vitro*, did not induce significant toxicity (Figure S17A). Consistently, *in vivo* studies in C57BL/6 mice showed that N1 was well tolerated at the effective dose of 1 mg/kg, as indicated by the stable body weight, while only the highest tested dose (30 mg/kg) induced a modest reduction (∼10%) compared to controls (Figure S17B). These findings indicate that N1 exerts anti-tumor activity at therapeutically relevant doses without appreciable toxic effects. We also elucidated the mechanism of action of N1 and identified ERAP1 as a direct target of this compound. Our findings not only establish ERAP1 as a critical player and druggable target to block the uncontrolled activation of the HH pathway but they also highlight the therapeutic potential of N1, a natural compound with precise efficacy and minimal toxicity. Overall, this work paves the way for next-generation treatments for HH-MB, offering hope for improved survival and quality of life for affected patients.

MATERIALS AND METHODS

Molecular docking

Docking simulations were carried out with the FRED docking program, version 3.0.1 (OpenEye, Cadence Molecular Sciences, Santa Fe, NM; http://www.eyesopen.com) using the default settings and the "High" docking resolution.[89,90] The X-ray crystallography structure of ERAP1 bound to the zinc aminopeptidase inhibitor bestatin (PDB: 3MDJ) was used as a rigid receptor.[53] The binding site was centered on the co-crystallized ligand within the catalytic site, and it had an outer shape of 762 Å^3. Conformational analysis of the compound library was achieved with Omega software version 3.1.0.3 (OpenEye, Cadence Molecular Sciences), allowing the storage of up to 600 conformers for each ligand[91] Visual inspection and drawings were carried out with an open-source build of the PyMOL Molecular Graphics System, version 2.2.0 (Schrödinger).

Chemistry

All the tested compounds (N1–N11) are known structures belonging to the in-house library of natural products available at the Organic Chemistry Laboratory of the Department of Chemistry and Technology of Drugs of Sapienza University (Rome, Italy). The chemical identity of compounds was assessed by rerunning NMR experiments and proved to agree with the literature data reported below for each compound:

Compound N1 (canthin-6-one or 1,6-diazatetracyclo[7.6.1.05,16.010,15]hexadeca-3,5(16),6,8,10,12,14-heptaen-2-one) showed NMR spectra identical to those reported in the literature.[92]

Compound N2 (coumaric acid or (E)-3-(4-hydroxyphenyl)prop-2-enoic acid) showed NMR spectra identical to those reported in the literature.[93]

Compound N3 (rhein or 4,5-dihydroxy-9,10-dioxoanthracene-2-carboxylic acid) was purchased from TCI (CAS: 478-43-3, Chuo-ku, Tokyo, Japan) and used without further purification.

Compound N4 (oleanolic acid or ((4aS,6aS,6bR,8aR,10S,12aR,12bR,14bS)-10-hydroxy-2,2,6a,6b,9,9,12a-heptamethyl-1,3,4,5,6,6a,6b,7,8,8a,9,10,11,12,12a,12b,13,14b-octadecahydropicene-4a(2H)-carboxylic acid) was purchased from Sigma-Aldrich (CAS: 508-02-1, St. Louis, MO) and used without further purification.

Compound N5 (sakuranetin or (±)-5-hydroxy-2-(4-hydroxyphenyl)-7-methoxy-2,3-dihydrochromen-4-one) showed NMR spectra identical to those reported in the literature.[94]

Compound N6 (ferruginin B or 4,5,10-trihydroxy-7-methyl-1,1,3-*tris*(3-methylbut-2-enyl)anthracen-2-one) showed NMR spectra identical to those reported in the literature.[30]

Compound N7 (luteolin or 2-(3,4-dihydroxyphenyl)-5,7-dihydroxychromen-4-one) showed NMR spectra identical to those reported in the literature.[95]

Figure 6. N1 suppresses the growth of primary HH-MB cells *in vitro*

Primary cell cultures of *Math1-Cre/Ptch1*$^{C/C}$ mice HH-MBs were treated with different amounts of N1. (A) Primary cells were counted with trypan blue at the indicated time points to evaluate the growth rate of viable cells. (B) Inhibition of cell proliferation measured as the percentage of BrdU uptake in N1-treated cells vs. DMSO used as control. (C) Representative images of BrdU uptake in primary HH-MB cells treated with N1 corresponding to the quantification shown in (B). (D) Percentage of cell death measured in the same cells as in (A). (E and F) Real-time quantification of apoptosis in primary HH-MB cells treated with increasing amounts of N1 using the IncuCyte Live Cell Analysis System with Annexin V (E) and Caspase-3/-7 (F) dyes. Annexin V or caspase-3/-7^{+} cells are expressed as fold change (FC) relative to time 0 (0 h) ± SD of $n = 3$ experiments. (G) Quantitative real-time PCR analysis of HH target and proliferation-related genes in primary HH-MB cells treated with the indicated doses of N1, normalized to *HPRT*. (H) Representative immunoblot of HH pathway components and apoptosis-related markers in the HH-MB cells analyzed in (G). (I) Densitometric analysis of the proteins shown in (H). (J) Quantitative real-time PCR of HH target genes and proliferation-related genes of primary HH-MB cells transduced with lentiviral particles encoding shCTR or shERAP1 and treated for 48 h with N1 or DMSO as control. Results are presented as mean (SD) from at least three independent experiments. Statistical analyses were performed using two-way ANOVA, unless otherwise specified, with treatment, time, gene, or protein as factors: (A) treatment F(3, 8) = 79.87, $p < 0{,}0001$; time F(3, 24) = 79.39, $p < 0.0001$; interaction F(9, 24) = 7.990, $p < 0.0001$; (B) one-way ANOVA, F(1.498, 2.997) = 552.6, $p = 0.0002$; (D) treatment F(3, 8) = 31.84, $p < 0.0001$; time F(2, 16) = 13.78, $p = 0.0003$; interaction F(6, 16) = 1.362, $p = 0.2881$; (E) treatment F(3, 8) = 222.8, $p < 0.0001$; time F(12, 96) = 617.5, $p < 0.0001$; interaction F(36, 96) = 29.67, $p < 0.0001$; (F) treatment F(3, 8) = 22.20, $p = 0.0003$; time F(12, 96) = 426.2, $p < 0.0001$; interaction F(36, 96) = 15.65, $p < 0.0001$; (G) treatment F(3, 45) = 49.69, $p < 0.0001$; gene F(4, 15) = 2.97, $p = 0.0544$; interaction F(12, 45) = 0.73, $p = 0.7118$; (I) treatment F(3, 42) = 7.39, $p = 0.0004$; protein F(6, 14) = 13.84, $p < 0.0001$; interaction F(18, 42) = 8.68, $p < 0.0001$; and (J) treatment F(3, 60) = 125.3, $p < 0.0001$; gene F(9, 20) = 66.79, $p < 0.0001$; interaction F(27, 60) = 14.69, $p < 0.0001$. Statistical significance vs. CTR is indicated as $^{*}p < 0.05$; $^{**}p < 0.01$; $^{***}p < 0.001$; $^{****}p < 0.0001$.

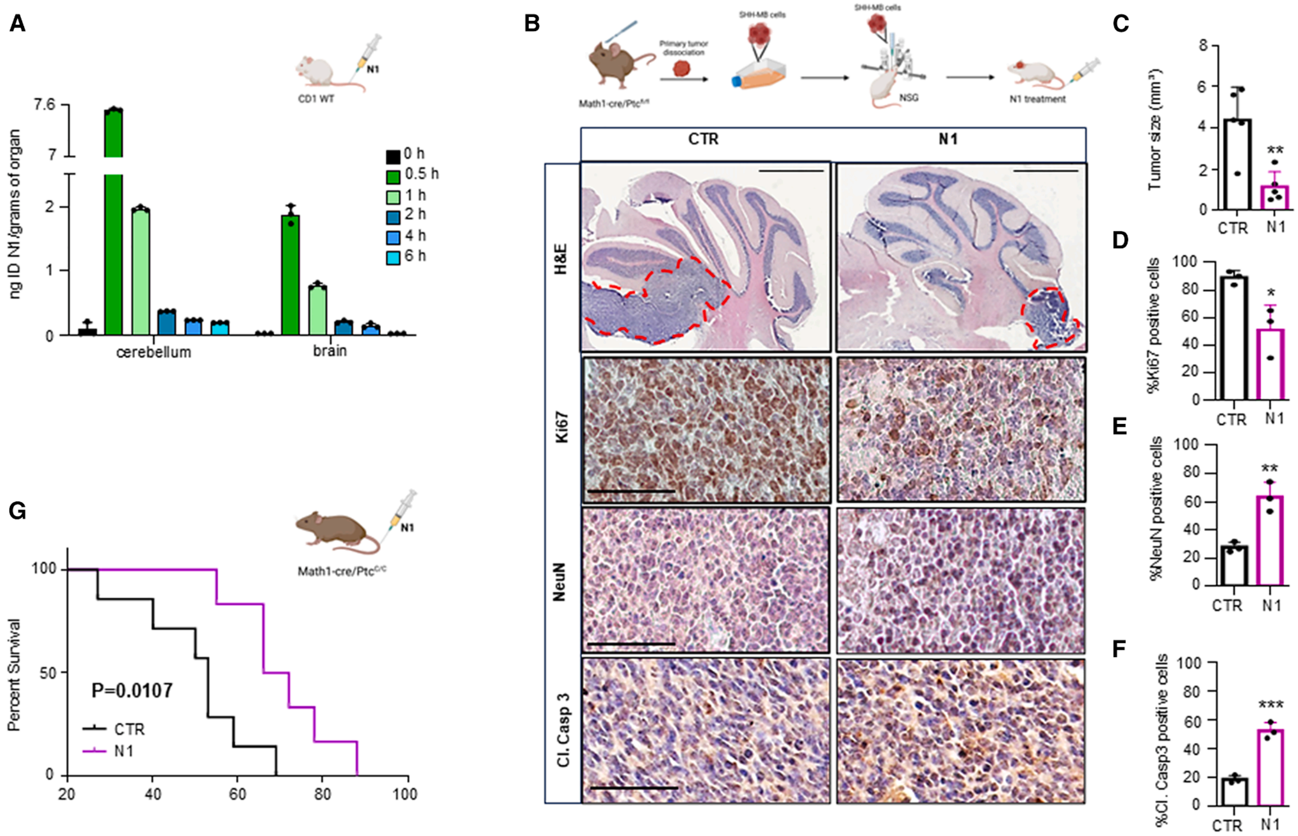

Figure 7. N1 crosses the BBB and inhibits the growth of primary HH-MB in an orthotopic implantation model

(A) The bar graph shows nanograms of N1 compound absorbed per gram of organ at different time points (0, 0.5, 1, 2, 4, and 6 h). Maximum absorption occurs at 0.5 h for both the brain and the cerebellum. At time zero, the quantified values are below the limit of quantification. (B) H&E (scale bar: 1 mm) and IHC staining for Ki67, NeuN, and cleaved caspase-3 in the explanted cerebellar tumor masses (scale bar: 50 μM). (C–F) Quantification of IHC staining shown in (B). Mean (SD); $*p < 0.05$; $**p < 0.01$; calculated with two-sided Student's *t* test. (G) Survival analysis by Kaplan-Meier curves and log rank (Mantel-Cox) test of *Math-Cre/Ptch1*$^{C/C}$ mice treated with N1 (1 mg/kg) or vehicle.

Compound N8 (catechin hydrate or (2R,3S)-2-(3,4-dihydroxyphenyl)-3,4-dihydro-2H-chromene-3,5,7-triol hydrate) showed NMR spectra identical to those reported in the literature.[96]

Compound N9 (*p*-methoxydihydrocinnamic acid or 3-(4-methoxyphenyl)propanoic acid) showed NMR spectra identical to those reported in the literature.[97]

Compound N10 (halfordinol or 4-(2-pyridin-3-yl-1,3-oxazol-5-yl)phenol) showed NMR spectra identical to those reported in the literature.[98]

Compound N11 (pilocarpine nitrate or (3S,4R)-3-ethyl-4-[(3-methylimidazol-4-yl)methyl]oxolan-2-one nitrate) showed NMR spectra identical to those reported in the literature.[99]

Chemicals and reagents

Optima MS-grade water, acetonitrile (ACN), methanol (MeOH), and isopropanol were purchased from Thermo Fisher Scientific (Waltham, MA). All reagents and salt were purchased from Merck (Darmstadt, Germany).

Cellular antigen processing assay

HeLa cells stably overexpressing H-2K^b were grown to 90% confluence in 12-well plates and transfected with the pTracer-CMV2-L13L construct encoding the L13L peptide and the GFP reporter for the detection of transfected cells. Lipofectamine 2000 (Life Technologies, Carlsbad, CA) was used as the transfection reagent, according to the manufacturer's protocol. After 6 h, cells were treated with increasing concentrations of ERAP1 inhibitors (5, 10, 30 μM) or Leu-SH (30 μM) for 48 h. Cells were then harvested and stained with the monoclonal antibody 25-D1.16, which recognizes the ovalbumin-derived peptide S8L bound to H-2K^b. The mean fluorescence intensity of the S8L-H-2K^b complex was assessed on the GFP$^+$ cell population by flow cytometry.

Cell and primary cultures

NIH 3T3 SHH-Light II cells, MEFs from WT or *Ptch1*$^{-/-}$ mice, Med1-MB, and HDMB03 were cultured in Dulbecco's modified Eagle's medium (DMEM; Sigma-Aldrich) plus 10% fetal bovine serum (FBS; Sigma-Aldrich). D283 was maintained in Eagle's minimum

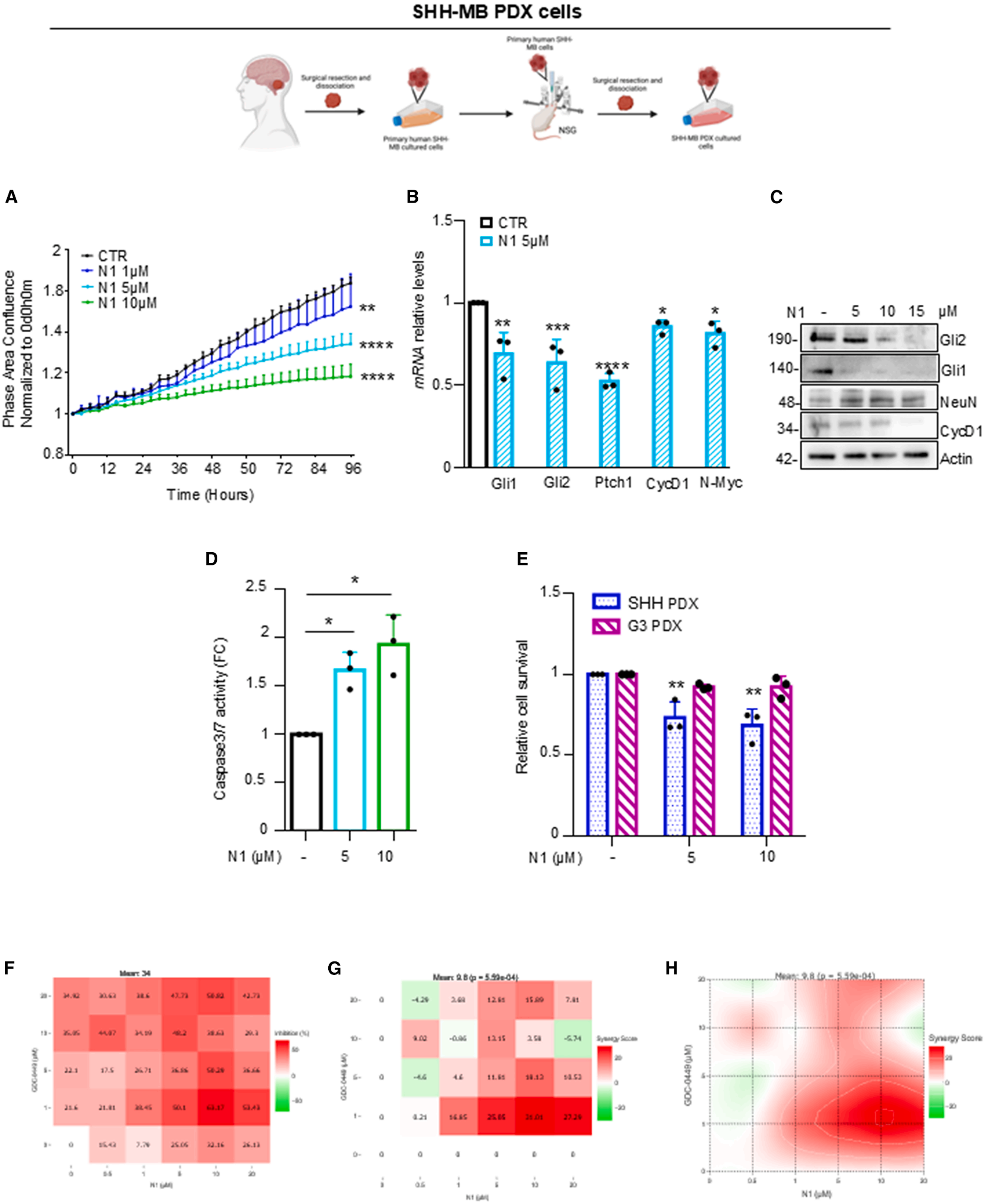

(legend on next page)

essential medium (Sigma-Aldrich) plus 20% FBS. CHLA cells were cultured in DMEM:F12 medium (American Type Culture Collection [ATCC] 30-2006) with 20 ng/mL human recombinant EGF, 20 ng/mL human recombinant basic FGF (bFGF), and 2% (v/v) B-27 supplement. All media contained 1% penicillin-streptomycin (P/S) and 1% L-glutamine (Sigma-Aldrich). ASZ001 BCC cells were cultured in 154CF medium (Gibco-BRL, Grand Island, NY) plus 2% FBS chelated with Chelex 100 sodium form (Sigma-Aldrich), calcium chloride 0.05 mM (Gibco-BRL) and 1% P/S. *Ptch1*$^{-/-}$ MEFs were a gift from Dr. M.P. Scott (Stanford, CA), and Med1-MB cells were a gift from the laboratory of Yoon-Jae Cho (Stanford, CA). D283 and HDMB03 were kindly provided by Dr. V. D'Angiolella. CHLAs (CRL-3021) were obtained from the ATCC.

For cerebellar GNP cultures from 5-day-old mice, cerebella were removed aseptically, cut into small pieces, and incubated at room temperature for 15 min in digestion buffer (Dulbecco's phosphate-buffered saline [PBS; Invitrogen, Gaithersburg, MD] with 0.1% trypsin, 0.2% EDTA, and 10 μg/mL DNase). Tissues were then triturated with fire-polished Pasteur pipettes to obtain a single-cell suspension. Cells were centrifuged and resuspended in neurobasal medium supplemented with B27 (2%), P/S (1%), and L-glutamine (1%) and plated at a density of 2×10^5 cells/cm^2.

Primary HH-MB cells were freshly isolated from *Math1-Cre/Ptch1*$^{C/C}$ mice. Briefly, the tumor was mechanically disrupted with fire-polished Pasteur pipettes in Hank's balanced salt solution with 1% P/S and treated with DNase (10 μg/mL) for 20 min. Cells were centrifuged and resuspended in neurobasal media-A (Sigma-Aldrich) with B27 supplement minus vitamin A (2%), P/S (1%), and L-glutamine (1%). Stable HH-dependent MB cells were cultured as neurospheres in DMEM/F12 media (2% B27 minus vitamin A, 3% glucose 10×, 0.2% insulin 10 mg/mL, 1% P/S, 0.01% heparin 2 mg/mL, and 0.06% *N*-acetyl-L-cysteine).

ICN-MB-PDX12 (SHH) and ICN-MB-PDX7 (G3) were derived from primary human MB tumors obtained from surgical resections at the Necker Hospital for Sick Children (Paris, France). All human samples were collected with informed consent from patients or their legal representatives, and all experimental procedures adhered to guidelines approved by the institutional review board at Necker Hospital.

Once established *in vivo*, PDX models were maintained through serial propagation in nude mice in compliance with the Animal Research: Reporting of *In Vivo* Experiments (ARRIVE) guidelines. For *in vitro* culture, tumors were dissociated using a solution containing neurobasal media, DNase I, collagenase P, collagenase/dispase, B27 supplement without vitamin A, and N2 supplement.

SHH-MB PDX cells were cultured in neurobasal media supplemented with B27 supplement without vitamin A, bovine serum albumin (BSA), *N*-acetyl cysteine, D-glucose, P/S, and L-glutamine. G3-MB PDX cells were maintained in neurobasal media supplemented with B27 supplement without vitamin A, N2 supplement, BSA, P/S, L-glutamine, human bFGF, and human EGF.

For drug treatment, SHH-MB PDX cells were cultivated in adherent conditions on dishes or multi-well plates that were pre-coated with poly-D-lysine (Millipore, Burlington, MA) and Matrigel Growth Factor Reduced (catalog no. 354230, Corning, Corning, NY).

Whenever necessary, neurosphere cultures were pelleted and dissociated by incubation with Accutase to obtain a single-cell suspension.

Mycoplasma contamination in cell cultures was routinely detected by using a PCR detection kit (Applied Biological Materials, Richmond, Canada).

Transfections and lentiviral infections

Transient transfections were performed using DreamFectGold transfection reagent (Oz Biosciences SAS, Marseille, France) in accordance with the manufacturer's protocols.

Lentiviral particles were generated in HEK293 cells by combining packaging plasmids pCMV-dR8.74 and VSV-G/pMD2, with pLKO.1 plasmid (shCTRL SHC002; shERAP1 TRCN0000031119, Sigma-Aldrich), using the calcium phosphate transfection method. *Ptch1*$^{-/-}$ MEFs were infected by the spin inoculation method, and primary MB cells were infected with purified lentiviral particles.

Plasmids, antibodies, and other reagents

pcDNA3.1-FLAG-USP47, FLAG-ERAP1, and HA-Gli1 was generated in our lab with standard cloning techniques and verified by

Figure 8. N1 impinges on SHH-MB PDX cell growth

(A) Tumor cells were seeded in 96-well tissue culture plates, and their proliferation was measured as phase area confluence normalized to point 0 and calculated using IncuCyte Zoom software from phase-contrast images. Cells were scanned every 3 h, from 0 to 96 h after the treatment. Graph shows data ± SD analyzed by using the IncuCyte software (Essen BioScience). (B and C) mRNA (B) and protein (C) expression levels of HH target genes of SHH-MB PDX cells treated with the indicated concentrations of N1 for 48 h. Results in (B) were normalized to endogenous control *GAPDH*. (D) Caspase-3/-7 activity in human SHH-MB PDX treated with N1 for 48 h at the indicated concentration. (E) Cell viability of SHH-MB PDX and G3-MB PDX cells after treatment with N1 for 48 h at the indicated concentrations. (F–H) Percentage of cell viability inhibition (F) and HSA model (G and H) showing the synergistic effect of combined N1 and GDC-0449 treatment in SHH-MB PDX calculated by https://synergyfinder.org/. Data are presented as mean (SD) from at least three independent experiments. Statistical analyses were performed using two-way ANOVA, unless otherwise specified, with treatment, time, gene, or subgroup as factors: (A) treatment F(3, 12) = 22.74, $p < 0.0001$; time F(32, 384) = 318.9, $p < 0.0001$; interaction F(96, 384) = 18.88, $p < 0.0001$; (B) treatment F(1, 10) = 139.1, $p < 0.0001$; gene F(4, 10) = 5.68, $p = 0.0119$; interaction F(4, 10) = 5.68, $p = 0.0119$; (D) one-way ANOVA, F(1.513, 3.027) = 23.10, $p = 00155$; and (E) treatment F(2, 6) = 11.90, $p = 0.0082$; MB subgroup F(1, 6) = 39.12, $p = 0.0008$; interaction F(2, 6) = 10.14, $p = 0.0119$. Statistical significance vs. SAG (A and C) or CTR (E, F, and H) is indicated as *$p < 0.05$; **$p < 0.01$; ***$p < 0.001$; ****$p < 0.0001$.

sequencing. shCTRL (SHC002) and shERAP1 (TRCN0000031119) in pLKO.1 plasmid were purchased from Sigma-Aldrich.

Mouse anti-Gli1 (L42B10, 1:500), rabbit anti-βTrCP (D13F10, 1:1,000), rabbit anti-cleaved caspase-3 (Asp175 D3E9, 1:100 for IHC, 1:500 for western bloting [WB]), rabbit anti-Nanog (D73G4 XP, 1:1,000), mouse anti-Oct4 (D705Z, 1:1,000), and rabbit anti-PARP (1:1,000) were purchased from Cell Signaling Technologies (Beverly, MA). Mouse anti-β-actin C4 horseradish peroxidase (HRP) (sc-47778, 1:2,000), mouse anti-vinculin 7F9 (sc-73614, 1:2,000), mouse anti-cyclin D2 DCS-3 (sc-56305, 1:1000), mouse anti-HA-probe F-7 HRP (sc-7392 HRP, 1:1,000), mouse anti-caspase-3 4i29 (sc-56050, 1:1,000), mouse anti-N-myc B8.4.B (sc-53993, 1:1,000), and mouse anti-βTrCP C-6 (sc-390629, 2 μg) were purchased from Santa Cruz Biotechnology (Dallas, TX). Goat anti-Gli3 (AF3690, 1:500), goat anti-Gli2 (AF3635, 1:1,000), and mouse anti-ERAP1 6H9 (MAB2334, 1:500) were purchased from R&D Systems (Minneapolis, MN). Anti-FLAG M2 HRP (A85921:2,000) was purchased from Sigma-Aldrich. Rabbit anti-SOX2 (1:1,000) was purchased by Abcam (Cambridge, UK). Phycoerythrin-cyanine7-conjugated mouse antibody against the $OVA_{257-264}$ (SIINFEKL) peptide bound to H-$2K^b$ (25-D1.16) was purchased from Thermo Fisher Scientific. Goat anti-mouse immunoglobulin G (IgG) HRP conjugated (1:5,000), goat anti-rabbit IgG HRP conjugated (1:5,000), and donkey anti-goat IgG HRP conjugated (1:5,000) were purchased by Bethyl Laboratories (Montgomery, TX).

Where indicated, cells were treated with SAG (200 nM, Alexis Biochemicals, Farmingdale, NY), cycloheximide (CHX; 100 μg/mL, Sigma-Aldrich), vismodegib (Selleckchem, Houston, TX) and GANT61 (Enzo Life Sciences, Exeter, UK) at the indicated concentrations.

Luciferase reporter assay

The HH-dependent luciferase assay was performed in NIH 3T3 SHH-Light II cells, stably expressing a Gli-RE and the pRL-TK Renilla (normalization control), treated for 48 h with SAG (200 nM) and N1, N3, N7, or N10 and/or DMSO as control at the indicated concentrations. Luciferase and Renilla activities were assayed with a dual-luciferase assay system according to the manufacturer's instructions (Biotium, Hayward, CA). Results were expressed as luciferase/Renilla ratios and represented the mean ± SD of at least three experiments, each performed in triplicate.

WNT and Jun luciferase assays were performed in MEFs transfected with Top Flash-luciferase reporter and β-catenin or MMP1-luciferase reporter and c-Jun, respectively, and treated with different concentrations of compound N1 or DMSO as a control for 48 h. Luciferase and Renilla activities were assayed with a dual-luciferase assay system according to the manufacturer's instructions (Biotium). Results were expressed as luciferase/Renilla ratios and represented the mean ± SD of at least three experiments, each performed in triplicate.

Immunoblot analysis and immunoprecipitation

Cells were lysed in a solution containing radioimmunoprecipitation assay (RIPA) buffer (50 mM Tris-HCl at pH 7.6, 150 mM NaCl, 0.5% sodium deoxycholic, 5 mM EDTA, 0.1% SDS, 100 mM NaF, 2 mM NaPPi, and 1% NP-40) supplemented with protease and phosphatase inhibitors. The lysates were centrifuged at 40,000 rpm for 20 min at 4°C and the resulting supernatants were resuspended in sample loading buffer, boiled for 5 min, resolved in SDS-PAGE, transferred to nitrocellulose membranes (GVS North America, Sanford, ME), blocked with 5% skim milk in Tris-buffered saline containing 0.1% Tween 20 (Sigma-Aldrich), and incubated with the indicated antibodies.

Immunoprecipitation was performed using whole-cell extracts obtained by lysing cell pellets with Triton X-100 buffer (50 mM Tris-HCl, pH 7.5, 250 mM sodium chloride, 50 mM sodium fluoride, 1 mM EDTA, pH 8, 0.1% Triton X-100), supplemented with protease and phosphatase inhibitors. Cell lysates were immunoprecipitated overnight at 4°C with rotation with specific primary antibodies or IgG used as a control (2 μg/mg, Santa Cruz Biotechnology). The day after, immunocomplexes were incubated with protein G agarose beads (Santa Cruz Biotechnology) for 1 h at 4°C with rotation. The immunoprecipitates were then washed five times with the lysis buffer described above, resuspended in sample loading buffer, boiled for 5 min, resolved in SDS-PAGE, and then subjected to immunoblot analysis. Additional pull-down experiments were carried out using *in vitro* translated FLAG-USP47 from pcDNA3.1-FLAG-USP47 plasmid and ERAP1 from pCMV6-XL5-ERAP1 (SC311137, Origene, Rockville, MD) plasmid by the TNT Quick Coupled Transcription/Translation System (Promega, Madison, WI). FLAG-USP47 and ERAP1 were placed in a 1:1 ratio into PC-100 binding buffer (HEPES, pH 7.4, 20 mM, $MgCl_2$ 2 mM, KCl 100 nM, glycerol 20%, EDTA 0.2 mM, IGEPAL 0.05%, BSA 100 mg/mL, and DTT 1 mM) supplemented with protease and phosphatase inhibitors and with N1 (1 μM) or vehicle as control. The protein mixture was immunoprecipitated overnight at 4°C with rotation with anti-ERAP1 6H9 (2 μg/mg, MAB2334, R&D Systems) or IgG used as a control (2 μg/mg, Santa Cruz Biotechnology). The day after, the immunocomplexes were analyzed as described above.

For all immunoblot analyses, immunoreactive bands were visualized by enhanced chemiluminescence using WesternBright enhanced chemiluminescence HRP substrate (Advansta or Cyanagen).

CETSA and ITDRF

For the CETSA assay, MEF protein extracts were freshly prepared in RIPA buffer (10 mM Tris HCl, pH 7.4, 150 mM NaCl, 1% IGEPAL, 1% sodium deoxycholate, 0.1% SDS, 0.1% glycerol, and 2 mM DTT), supplemented with protease and phosphatase inhibitors. Homogenization was performed by three cycles of freezing and thawing in dry ice. The soluble fraction was separated from debris. The cell lysate was divided into two tubes: the first half was treated with N1, N3, or N7 (1 μM), and the second half was exposed to vehicle only (control). After a 30-min incubation at room temperature, lysates were further divided into smaller aliquots (400 μg each) and heated individually at the reported temperatures for 3 min, followed by 3 min cooling at room temperature. Then, they were centrifuged to separate the soluble fractions from precipitates. All supernatants were analyzed by WB. For the ITDRF assay, MEF protein extracts were freshly prepared using the same lysis buffer described above. The cell lysate was equally divided into six tubes: five were treated with an increasing amount of N1 (1, 10, 100, 1,000, 5,000 nM), and the sixth was exposed to vehicle only (control). After a 30-min incubation at room temperature, lysates were heated at 62°C, according to the results obtained in the CETSA assay, for 3 min followed by 3 min of cooling at room temperature. Then, they were centrifuged to separate the soluble fractions from precipitates. All supernatants were analyzed by WB.

Expression, purification, and quality control of recombinant ERAP1

ERAP1 expression plasmid was kindly provided by Nicola Burgess-Brown (Addgene plasmid no. 39174; http://n2t.net/addgene:39174; RRID: Addgene_39174). Recombinant bacmid was obtained via transposition using *Escherichia coli* DH10EmBacY cells (kindly provided by Imre Berger, University of Bristol, Bristol, UK) and used for baculovirus generation in Sf9 cells (Expression Systems, Davis, CA). The protein was expressed in the secreted form in Hi5 cells (Expression Systems) and purified from the medium after 72 h post-infection. One liter of human recombinant ERAP1-containing medium was concentrated to 200 mL by diafiltration using a 10-kDa molecular weight cutoff crossflow protein concentration cassette (Pierce, Thermo Scientific), and then incubated with 1 mL Ni Sepharose excel resin (Cytiva, Marlborough, MA) for 2 h at 4°C. The slurry was loaded on a gravity column that after extensive washing with Tris buffer 50 mM, pH 8, 10 mM imidazole, 0.5 M NaCl, and 10% glycerol was eluted with the same buffer containing 300 mM imidazole. His-tag was removed by homemade tobacco etch virus protease during an overnight dialysis step in 20 mM HEPES, pH 7.4, 200 mM NaCl, and 0.5 mM Tris(2-carboxyethyl)phosphine (TCEP). The untagged protein was recovered using negative affinity and further purified on a 5-mL HiTrap Q HP column (Cytiva) over a linear gradient with a buffer of 20 mM HEPES, pH 7.4, 0.5 mM TCEP, and 1 M NaCl. Fractions containing ERAP1 were concentrated and loaded onto a Superdex 200 16/60 column equilibrated with 20 mM HEPES, pH 7.4, 0.15 M NaCl, 0.5 mM TCEP, and 5% glycerol. The final protein was concentrated to 20 mg/mL, flash-frozen, and stored at −80°C. The protein quality was evaluated by SDS-PAGE gel, TSA, and MP (Refeyn, Waltham, MA) as described in Figure S7.

SAXS data collection and analysis

In setting up the SAXS measurements, ERAP1 and ERAP1 in complex with N1 were individually purified by size-exclusion chromatography exploiting a Superdex 200 10/300 GL column. The buffer used as mobile phase for ERAP1 alone during the SAXS measurements was composed of HEPES 10 mM, pH 7.4, NaCl 150 mM, and glycerol 5% v/v. In addition, for the complex ERAP1/N1, we used the same buffer as the mobile phase added with 300 μM N1. Prior to the chromatography run, ERAP1 was incubated on ice with 300 μM N1 for 30 min. The fractions corresponding to the elution peaks were pooled and used in the SAXS experiment. The protein samples used for data collection had a final concentration of 3.5 mg/mL for ERAP1 and 1.57 mg/mL for the ERAP1/N1 complex. Data for both samples were collected by exposing the single protein and the complex, with 10 exposures of 1 s each, with temperature control fixed at 20°C. The corresponding buffer scattering signal was measured before and after each sample, and the average scattering signal was subtracted from the protein scattering curves. The one-dimensional scattering profiles were obtained by subtracting the buffer average from the ERAP1 and ERAP1/N1 scattering curves using the ATSAS software package[100] to start the *ab initio* model reconstructions, the Guinier analysis, and the pair distance distribution (P(r)) function. The *ab initio* models of ERAP1 and ERAP1/N1 were generated using the DAMMIF software,[101] while the P(r) functions were calculated by the program GNOM.[102]

In situ PLA

For the *in situ* visualization of protein-protein interactions, we followed the Duolink PLA fluorescence protocol (Sigma-Aldrich) using the Duolink *In Situ* Detection Reagents Orange Kit (catalog no. DUO92007, Sigma-Aldrich). Briefly, after fixation with 4% paraformaldehyde for 15 min and permeabilization with 0.2% PBS-Triton X-100 at room temperature for 10 min, the cells were blocked in a drop of blocking solution (Sigma-Aldrich) at 37°C for 1 h and incubated with primary antibodies that were diluted in Duolink antibody diluent (Sigma-Aldrich) in a humidity chamber. Following washing in wash buffer A (10 mM Tris, 150 mM NaCl, and 0.05% Tween 20), cells were incubated with secondary antibodies conjugated with PLUS and MINUS probes (Sigma-Aldrich) for 1 h at 37°C. The following Duolink *in situ* PLA secondary antibodies were used: Anti-Mouse MINUS (catalog no. DUO92004), and Anti-Rabbit PLUS (catalog no. DUO92002). Next, the cells were again washed twice in wash buffer A and then incubated with the ligase (diluted 1:40 in ligation buffer) for 30 min at 37°C. Following the next round of washing in wash buffer A, cells were incubated with the polymerase (diluted 1:80 in an amplification buffer) for 100 min at 37°C. Finally, the cells were washed in wash buffer B (200 mmol/L Tris and 100 mmol/L NaCl), counterstained with DAPI (0.5 μg/mL, Sigma-Aldrich), mounted in fluorescence mounting medium (Dako, Agilent Technologies, Denmark), and allowed to dry before imaging. Negative controls were performed using only secondary antibodies.

In vivo ubiquitylation assay

MEFs were lysed with a denaturing buffer (1% SDS, 50 mM Tris-HCl at pH 7.5, 0.5 mM EDTA, 1 mM DTT) to disrupt protein-protein interactions. Lysates were then diluted 10 times with NETN buffer (100 mM NaCl, 20 mM Tris-HCl, pH 8.0, 0.5 mM EDTA, 0.5% NP40) and subjected to immunoprecipitation with anti-βTrCP (Santa Cruz Biotechnology) overnight at 4°C with rotation. The immunoprecipitated proteins were then washed five times with the NETN buffer, resuspended in sample loading buffer, boiled for 5 min, resolved in SDS-PAGE, and then subjected to immunoblot analysis. Polyubiquitylated forms were detected using mouse anti-HA from Santa Cruz Biotechnology.

Cell proliferation and cell death assays

For Med1 and MB cells, trypan blue count was performed after treatment periods of 24, 48, and 72 h with N1 at the indicated dose. For IncuCyte experiments, cells were seeded in 96-well plates (Corning, catalog no. 353072; 3×10^3 cells/well for Med1; 12×10^3 cells/well for HH-MB; 10×10^4 cells/well for SHH-MB PDX; 6 wells for each condition) in complete medium and treated with N1 or DMSO as control. Where indicated, MB cells were treated with IncuCyte Caspase-3/-7 Green Dye (catalog no. 4440, Sartorius, Göttingen, Germany) and IncuCyte Annexin V NIR Dye (catalog no. 4768, Sartorius) to assess cell viability. Plates were transferred into the IncuCyte Live Cell Analysis Systems and incubated at physiological conditions (37°C, 5% CO_2) over 72 h after treatment. Images were collected once per day for Med1, every 12 h for HH-MB, and every 3 h for SHH-MB PDX; proliferation was evaluated as phase area confluence (%) normalized to scans obtained at time 0 (0 h) and expressed as fold change (FC) ± SD of $n = 3$ experiments. Data were analyzed by using the IncuCyte software package (Essen BioScience, Ann Arbor, MI). Cell viability of HeLa-K^b cells, primary HH-MB murine cells, and SHH-MB PDX cells after ERAP1 inhibitor treatment was tested *in vitro* using the CellTiter-Glo Assay (Promega), as per the manufacturer's protocol. For HH-MB cells, 15×10^4 cells were seeded on a 96-well plate (Corning, catalog no. 353072), in 100 μL culture medium. After 48 h of treatment, cells were lysed by adding 1 volume of the properly prepared reagent from the kit. We transferred 100 μL lysate to an opaque-white flat-bottom 96-well plate (Corning, catalog no. 3355) for luminescence measurement using a luminometer (Tristar 3 Multimode Reader, Berthold Technologies, Oak Ridge, TN). Synergy/antagonism scores for *in vitro* combinatorial drug treatment were calculated using SynergyFinder software and CellTiter-Glo data as input, following the highest single agent (HSA) model.

Caspase-3/-7 activity in an N1-treated human SHH-MB PDX model was measured using the Caspase-Glo 3/7 Assay System (Promega, catalog no. G8091) according to the manufacturer's instructions.

mRNA expression analysis

Total RNA was extracted using the RNeasy Plus Mini Kit (QIAGEN, Hilden, Germany) for MONO-exonic genes or TRIzol reagent (Thermo Fisher Scientific) and reverse transcribed with the SensiFAST cDNA Synthesis Kit (Bioline Reagents Limited, London, UK). Reverse quantitative polymerase chain reaction analysis of *Gli1*, *Gli2*, *CyclinD2*, *HHIP1*, *N-Myc*, *Patched1*, *Nanog*, and *POU5F1* (OCT4) mRNA expression was performed using the ViiA 7 Real-Time PCR System (Life Technologies). Standard quantitative real-time PCR thermal cycler parameters were used to amplify a reaction mixture containing cDNA template and SensiFAST Probe Lo-ROX Mix (Bioline Reagents Limited) and TaqMan gene expression assays (Thermo Fisher Scientific). The average of two threshold cycles was used to calculate the amount of transcript in each sample amplified in triplicate (using SDS version 2.3 software). mRNA quantification was calculated as the ratio of the sample quantity to the calibrator quantity expressed in arbitrary units. Data were normalized with the endogenous control (*HPRT*) and expressed as the FC with respect to the control sample value.

The following primers were used to amplify the indicated genes:

mGli1 forward 5′-GCC AAC TTT ATG TCA GGG TCC CAG-3′
mGli1 reverse 5′-GGA GAG AGC CCG CTT CTT TGT TAA-3′
mGli2 forward 5′-CAG CCA CCC CAG CGT AGA CA-3′
mGli2 reverse 5′-GCC CCA GGT CGC ACT CTA G-3′
mCycD2 forward 5′-AGA AGG ACA TCC AAC CGT ACA TG-3′
mCycD2 reverse 5′-CAT GGC CAG AGG AAA GAC CTC-3′
mHPRT forward 5′-GCT TCC TCC TCA GAC CGC TT-3′
mHPRT reverse 5′-GGT CAT AAC CTG GTT CAT CAT GG-3′

TaqMan gene expression assays (Thermo Fisher Scientific) were used to amplify the following genes:

mPtch1 Mm00436026_m1
mHHIP1 Mm00469580_m1
mMycn Mm00476449_m1
mNanog Mm02019550_s1
mPou5f1 (OCT4) Mm03053917_g1
mHPRT Mm03024075_m1
hGli1 Hs00171790_m1
hGli2 Hs01119974_m1
hPtch1 Hs001811117_m1
hCycD1 Hs00765553_m1
hMycN Hs002332074_m1
hGapdh Hs02786624_g1

BrdU and EdU incorporation and MB-neurosphere-forming assay

Cell proliferation was evaluated by BrdU (Roche, Welwyn Garden City, UK) or EdU (Thermo Fisher Scientific) detection. Briefly, cells were pulsed for 24 h with BrdU or EdU and then fixed with 4% paraformaldehyde and permeabilized with 0.2% PBS-Triton X-100. Nuclei were counterstained with Hoechst reagent, and fluorescence detection was performed according to the manufacturer's instructions. At least 500 nuclei were counted in triplicate, and the number of $BrdU^+$ and EdU^+ nuclei was recorded.

For the neurosphere-forming assay, MB-SLCs were plated in 96-well plates in decreasing numbers (50, 25, 10, 5 cells; 12 wells for each condition, 10 replicates per cell/density number) in neurosphere culture media and treated with the indicated concentration of N1. The plates were incubated in a 37°C, 5% CO_2, humidified incubator. At 10 days, any well that contained neurospheres was scored.

Extreme limiting dilution analysis was conducted using the software available at https://bioinf.wehi.edu.au/software/elda/.

Animal studies

For the allograft experiment, Med1-MB cells (2×10^6) were injected s.c. at the posterior flank of NSG mice (Charles River Laboratories, Lecco, Italy). Tumors were grown until they were a median size of ~100 mm^3. Animals were randomly divided into two groups ($n = 6$) and intratumorally injected every other day with 1 mg/kg N1 and/or vehicle for 28 days. Cells were resuspended in an equal volume of culture medium and Matrigel (BD Biosciences, Heidelberg, Germany) before the s.c. injection. After the injection, tumor growth was monitored and measured with a caliper. Changes in tumor volume were evaluated with the formula (length × width) × 0.5 × (length + width).

Moreover, spontaneous MB from *Math1-Cre/Ptch1*$^{C/C}$ mice was isolated, minced, and pipetted to obtain a single-cell suspension. Equal amounts of cells (2×10^6) were injected s.c. at the posterior flank of NSG mice (Charles River Laboratories). Tumors were grown until they were a median size of ~200 mm^3. Animals were randomly divided into two groups ($n = 6$) and intratumorally injected every other day with 1 mg/kg N1 and/or vehicle for 17 days. Cells were resuspended in an equal volume of culture medium and Matrigel (BD Biosciences) before the s.c. injection. After the injection, tumor growth was monitored and measured with a caliper. Changes in tumor volume were evaluated with the formula (length × width) × 0.5 × (length + width).

For the orthotopic allograft model, adult NSG mice were anesthetized by intraperitoneal injections of ketamine (10 mg/kg) and xylazine (100 mg/kg). The posterior cranial region was shaved and placed in a stereotaxic head frame, and primary cells of spontaneous MB from freshly isolated *Math1-Cre/Ptch1*$^{C/C}$ mice were stereotaxically implanted into the cerebellum (2×10^5/3 μL) according to the atlas of Franklin and Paxinos coordinates. After injection, at an infusion rate of 1 μL/min, the cannula was kept in place for 5 min, and then the skin was closed using metallic clips. At 10 days following tumor implantation, the animals were randomly divided into two groups ($n = 6$) and treated i.v. every other day with 1 mg/kg N1 or vehicle only. After 25 days of treatment, animals were sacrificed, and their brains were fixed in 4% formaldehyde and paraffin embedded. Tumor volume calculation was performed on serial 60 coronal sections of 5 μm after H&E staining every 75 μm of brain slice. A microscope (Axio Imager M1 microscope, Leica Microsystems GmbH, Wetzlar, Germany) equipped with a motorized stage and Image Pro Plus 6.2 software was used to evaluate the tumor area of each slide. The tumor volume was calculated by the formula tumor volume = sum of measured area for each slice × slice thickness × sampling frequency.

For *Gfap-Cre/Ptch1*$^{C/C}$ mice injection, symptomatic mice were randomly divided into two groups ($n = 5$) and injected s.c. under the scruff with 1 mg/kg N1 or vehicle. After 24 h of treatment, tumor masses were explanted and analyzed by quantitative real-time PCR and immunoblotting analysis.

For survival analysis, P21 *Math-Cre/Ptch1*$^{C/C}$ mice were randomized to receive either N1 (1 mg/kg) or vehicle twice per week by i.v. injection.

For toxicity experiments, 4-week-old C57BL/6 mice were treated every 3 days i.v. for 4 weeks at the indicated concentration of N1.

All animal protocols were approved by local ethics authorities (Ministry of Health) and conducted in accordance with Italian governing law (D.lgs 26/2014). We followed the European and national regulations for the care and use of animals to protect them for experimental and other scientific purposes (D.lgs 26/2014). The study is also in compliance with ARRIVE guidelines.

IHC

Formalin-fixed paraffin-embedded (FFPE) tissues were cut into 5-μm sections for Ki67, NeuN, and cleaved caspase-3 IHC staining. FFPE slides were deparaffinized and subjected to heat-induced antigen retrieval at low or high pH buffer. Slides were blocked for 10 min with Super Block solution (ScyTek Mouse to Mouse HRP Staining System MTM001). FFPE slides were incubated with monoclonal antibodies against Ki67, NeuN, and cleaved caspase-3 (overnight 4°C). This step was followed by incubation for 20 min with secondary antibodies coupled with peroxidase (ScyTek, Logan, UT). Bound peroxidase was detected with diaminobenzidine (DAB) solution and DAB substrate buffer containing peroxide (ScyTek). Cell quantification was performed on collected sections using the imaging software NIS-Elements BR 4.00.05 (Nikon Instruments Europe, Campi Bisenzio, Italy).

UHPLC-MS/MS analysis

Extraction procedure

The brain and cerebellum samples (500 mg), previously stored at −80°C for 24 h, were homogenized with 1 mL PBS using an ultrasound probe (20% pulse, 6 min). A solution of $ZnSO_4$ 0.1 M in H_2O (1 mL) and ACN for HPLC (1 mL) was added to the mixture, which was further homogenized with ultrasound for 15 min. Subsequently, the homogenized brain was agitated using a vortex for 1 h at room temperature and then centrifuged at 3,000 × *g* for 5 min at 4°C. The supernatants were recovered and desalted following the protocol previously described,[103] using solid-phase extraction (SPE) C18 cartridges (Bond Elut 1 cm^3 LRC-C18, Varian, Palo Alto, CA), canthin-6-one was eluted from the SPE column with 500 μL ACN/H_2O (70/30, v/v) containing 0.1% trifluoroacetic acid and dried in a SpeedVac

SC250 Express (Thermo Savant, Holbrook, NY) to a final volume of 50 µL. Then, an isotopically labeled internal standard (C_{13} labeled caffeine, 5 ng/µL) was introduced. Subsequently, appropriate solvents were added to achieve a final composition of 200 µL 80:20 H_2O/MeOH v/v.

UHPLC-MS/MS analysis

The UHPLC-MS/MS analysis was conducted using a Vanquish binary pump H system (Thermo Fisher Scientific). The system was equipped with a thermostatted autosampler and column compartment, employing a C_8 Hypersyl GOLD column (100 × 2.1 mm, 1.9 µm particle size; Thermo Fisher Scientific) at 60°C, with a flow rate of 500 µL min^{-1}. The mobile phases included H_2O (referred to as phase A) and MeOH (referred to as phase B), both with 0.02% CH_3COOH and 5 mM CH_3COONH_4. The chromatographic gradient comprised 5 min at 30% phase B, a linear increase from 30% to 99% phase B over 15 min, 10 min at 99% phase B for washing, a rapid decrease from 99% to 30% phase B in 1 min, followed by 5 min at 30% phase B for equilibration. The injection volume was 10 µL.

The UHPLC system was coupled to the Q Exactive hybrid quadrupole-Orbitrap mass spectrometer (Thermo Fisher Scientific). The source settings included a spray voltage of 3.5 kV (electrospray ionization, ESI(+)) and 2.5 kV (ESI(−)), capillary temperatures of 275°C (ESI(+)) and 320°C (ESI(−)), sheath gas flow rates of 55 (ESI(+)) and 35 (ESI(−)) arbitrary units (a.u.), an auxiliary gas flow rate of 15 a.u., and auxiliary gas heater temperatures of 450°C (ESI(+)) and 400°C (ESI(−)). Full-scan MS data were acquired in the 200- to 1,200-*m/z* range, with a resolution (full width at half-maximum [FWHM]) of 70,000. The isolation window width was 2 *m/z*. For TOP 5 data-dependent acquisition MS/MS fragmentation, a resolution (FWHM) of 35,000 was used. The automatic gain control (AGC) target value was set at 100,000, and dynamic exclusion was set to 3 s. Collision energy fragmentation was achieved in the higher-energy collisional dissociation cell at 80 normalized collision energy. Raw data files were acquired using Xcalibur software (version 3.1, Thermo Fisher Scientific). All samples were analyzed in triplicate.[104]

The UHPLC-MS/MS method was validated following FDA guidelines using a brain and cerebellum control pool. The method was validated in matrix (a pool of control white samples). Specifically, recoveries were calculated in brain and cerebellum pools at three different concentrations (low, 0.02 pg/µL; medium, 1 pg/µL; high, 100 pg/µL), and intra-day and inter-day precision were assessed by evaluating the relative standard deviation (RSD%), matrix effect, and the minimum limits of quantification and of identification. Calibration curves were then constructed in matrix separately for the brain and cerebellum. All the results were in accordance with the guidelines and are shown in Table S1 and Figure S13.

Statistical analysis

For all experiments, statistical significance was assessed using one-way or two-way ANOVA, and, where appropriate, a two-sided Student's *t* test. Results are expressed as mean (SD) from an appropriate number of experiments (at least three biological replicates). Statistical significance was set at $p < 0.05$. Statistical analyses were performed using GraphPad Prism software (version 8.0, San Diego, CA). Data from IncuCyte experiments were analyzed with the IncuCyte software package.

DATA AND CODE AVAILABILITY

All data generated in this study are available within the article and supplemental information or from the corresponding authors on reasonable request.

ACKNOWLEDGMENTS

This paper was supported by the Fondazione AIRC (Associazione Italiana per la Ricerca sul Cancro) grant nos. IG20801 and IG29329 to L.D.M., IG24345 to D.F., MFAG 2021-ID 26536 to P.I., and IG23099 to F.S.; a Progetti di Ricerca di Università Sapienza di Roma grant to L.D.M.; Italian Ministry of Health grant nos. PRIN 2022MXFLMZ and P2022JZ9RE to L.D.M.; an Institut Pasteur/Cenci Bolognetti Foundation grant to L.D. M.; NextGenerationEU" DD. 3175/2021 E DD. 3138/2021 CN_3: National Center for Gene Therapy and Drugs based on RNA Technology Codice Progetto CN 00000041; NextGenerationEU ECS 0000024 Rome Technopole CUP B83C22002820006; a PNCSA-LUTE-D3-4-HEALTH-SPOKE-3/Ministery of Univeristy and Research grant to L.D.M.; and Dipartimenti di Eccellenza-L. 2023-2027. F.B. was supported by NextGenerationEU" DD. 3175/2021 E DD. 3138/2021 CN_3: National Center for Gene Therapy and Drugs based on RNA Technology Codice Progetto CN 00000041. L.L.S. and S.D.A. were supported by a Fondazione Veronesi fellowship for Italy. I.B. was supported by an Institute Pasteur Italy/Fondazione Cenci Bolognetti fellowship for study abroad. M.M. wishes to thank OpenEye Cadence Molecular Sciences for their free academic license.

AUTHOR CONTRIBUTIONS

Conceptualization, L.D.M., F.B., A.C., M.M., and D.F.; data curation, L.D.M., M.M., and D.F.; formal analysis, F.A., I.B., L.L.S., P.I., M.S.S., and M.M.; funding acquisition, L.D. M., D.F., P.I., and F.S.; investigation, I.B., D.Q., G.F., F.A., A.L.C., C.M.M., L.L.S., P.T., S.D., F.J., M.S.S., S.N., M.C., R.B., F.S., S.G., P.S., F.G., O.A., A.L., P.I., B.B., M.M., D.F., and L.D.M.; methodology, S.C., I.B., F.A., P.T., F.S., F.J., M.S.S., M.C., S.G., P.S., and M. M.; project administration, L.D.M.; resources, L.D.M., D.F., O.A., A.L., and M.M.; supervision, L.D.M.; B.B., M.M., D.F., and F.L.; validation, F.A., I.B., and L.L.S.; visualization, F.B., A.C., S.C., F.A., I.B., A.L.C., M.S.S., and S.G.; writing – original draft, L.D.M., F.B., A.C., D.F., and M.M.; writing – review & editing, L.D.M., F.B., and D.F. All authors read and approved the manuscript and agree to be accountable for all aspects of the research in ensuring that the accuracy or integrity of any part of the work is appropriately investigated and resolved.

DECLARATION OF INTERESTS

The authors declare no competing interests.

SUPPLEMENTAL INFORMATION

Supplemental information can be found online at https://doi.org/10.1016/j.ymthe.2025.10.036.

REFERENCES

1. Ramaswamy, V., and Taylor, M.D. (2017). Medulloblastoma: From Myth to Molecular. JCO *35*, 2355–2363. https://doi.org/10.1200/JCO.2017.72.7842.
2. Briscoe, J., and Thérond, P.P. (2013). The mechanisms of Hedgehog signalling and its roles in development and disease. Nat. Rev. Mol. Cell Biol. *14*, 416–429. https://doi.org/10.1038/nrm3598.
3. Clark, V.E., Erson-Omay, E.Z., Serin, A., Yin, J., Cotney, J., Özduman, K., Avşar, T., Li, J., Murray, P.B., Henegariu, O., et al. (2013). Genomic Analysis of Non- *NF2* Meningiomas Reveals Mutations in *TRAF7* , *KLF4* , *AKT1* , and *SMO*. Science *339*, 1077–1080. https://doi.org/10.1126/science.1233009.
4. Jones, S., Zhang, X., Parsons, D.W., Lin, J.C.-H., Leary, R.J., Angenendt, P., Mankoo, P., Carter, H., Kamiyama, H., Jimeno, A., et al. (2008). Core Signaling

Pathways in Human Pancreatic Cancers Revealed by Global Genomic Analyses. Science *321*, 1801–1806. https://doi.org/10.1126/science.1164368.

5. Caro, I., and Low, J.A. (2010). The Role of the Hedgehog Signaling Pathway in the Development of Basal Cell Carcinoma and Opportunities for Treatment. Clin. Cancer Res. *16*, 3335–3339. https://doi.org/10.1158/1078-0432.CCR-09-2570.
6. Raducu, M., Fung, E., Serres, S., Infante, P., Barberis, A., Fischer, R., Bristow, C., Thézénas, M.L., Finta, C., Christianson, J.C., et al. (2016). SCF (Fbxl17) ubiquitylation of Sufu regulates Hedgehog signaling and medulloblastoma development. EMBO J. *35*, 1400–1416. https://doi.org/10.15252/embj.201593374.
7. Ruiz I Altaba, A., Sánchez, P., and Dahmane, N. (2002). Gli and hedgehog in cancer: tumours, embryos and stem cells. Nat. Rev. Cancer *2*, 361–372. https://doi.org/10.1038/nrc796.
8. Bhatia, N., Thiyagarajan, S., Elcheva, I., Saleem, M., Dlugosz, A., Mukhtar, H., and Spiegelman, V.S. (2006). Gli2 Is Targeted for Ubiquitination and Degradation by β-TrCP Ubiquitin Ligase. J. Biol. Chem. *281*, 19320–19326. https://doi.org/10.1074/jbc.M513203200.
9. Huntzicker, E.G., Estay, I.S., Zhen, H., Lokteva, L.A., Jackson, P.K., and Oro, A.E. (2006). Dual degradation signals control Gli protein stability and tumor formation. Genes Dev. *20*, 276–281. https://doi.org/10.1101/gad.1380906.
10. Pan, Y., Bai, C.B., Joyner, A.L., and Wang, B. (2006). Sonic hedgehog Signaling Regulates Gli2 Transcriptional Activity by Suppressing Its Processing and Degradation. Mol. Cell. Biol. *26*, 3365–3377. https://doi.org/10.1128/MCB.26.9.3365-3377.2006.
11. Jiang, M.-X., and Zhou, Y.-J. (2008). Canthin-6-one alkaloids from *Picrasma quassioides* and their cytotoxic activity. J. Asian Nat. Prod. Res. *10*, 1009–1012. https://doi.org/10.1080/10286020802277956.
12. Infante, P., Faedda, R., Bernardi, F., Bufalieri, F., Lospinoso Severini, L., Alfonsi, R., Mazzà, D., Siler, M., Coni, S., Po, A., et al. (2018). Itch/β-arrestin2-dependent non-proteolytic ubiquitylation of SuFu controls Hedgehog signalling and medulloblastoma tumorigenesis. Nat. Commun. *9*, 976. https://doi.org/10.1038/s41467-018-03339-0.
13. Humke, E.W., Dorn, K.V., Milenkovic, L., Scott, M.P., and Rohatgi, R. (2010). The output of Hedgehog signaling is controlled by the dynamic association between Suppressor of Fused and the Gli proteins. Genes Dev. *24*, 670–682. https://doi.org/10.1101/gad.1902910.
14. Wang, B., and Li, Y. (2006). Evidence for the direct involvement of βTrCP in Gli3 protein processing. Proc. Natl. Acad. Sci. USA *103*, 33–38. https://doi.org/10.1073/pnas.0509927103.
15. Rusert, J.M., Wu, X., Eberhart, C.G., Taylor, M.D., and Wechsler-Reya, R.J. (2014). SnapShot: Medulloblastoma. Cancer Cell *26*, 940–940.e1. https://doi.org/10.1016/j.ccell.2014.11.015.
16. Robbins, D.J., Fei, D.L., and Riobo, N.A. (2012). The Hedgehog Signal Transduction Network. Sci. Signal. *5*, re6. https://doi.org/10.1126/scisignal.2002906.
17. Pak, E., and Segal, R.A. (2016). Hedgehog Signal Transduction: Key Players, Oncogenic Drivers, and Cancer Therapy. Dev. Cell *38*, 333–344. https://doi.org/10.1016/j.devcel.2016.07.026.
18. Fruci, D., Ferracuti, S., Limongi, M.Z., Cunsolo, V., Giorda, E., Fraioli, R., Sibilio, L., Carroll, O., Hattori, A., Van Endert, P.M., and Giacomini, P. (2006). Expression of Endoplasmic Reticulum Aminopeptidases in EBV-B Cell Lines from Healthy Donors and in Leukemia/Lymphoma, Carcinoma, and Melanoma Cell Lines. J. Immunol. *176*, 4869–4879. https://doi.org/10.4049/jimmunol.176.8.4869.
19. Fruci, D., Giacomini, P., Nicotra, M.R., Forloni, M., Fraioli, R., Saveanu, L., Van Endert, P., and Natali, P.G. (2008). Altered expression of endoplasmic reticulum aminopeptidases ERAP1 and ERAP2 in transformed non-lymphoid human tissues. J. Cell. Physiol. *216*, 742–749. https://doi.org/10.1002/jcp.21454.
20. Tempora, P., D'Amico, S., Gragera, P., Damiani, V., Krol, K., Scaldaferri, V., Pandey, K., Chung, S., Lucarini, V., Giorda, E., et al. (2024). Combining ERAP1 silencing and entinostat therapy to overcome resistance to cancer immunotherapy in neuroblastoma. J. Exp. Clin. Cancer Res. *43*, 292. https://doi.org/10.1186/s13046-024-03180-y.
21. Bufalieri, F., Infante, P., Bernardi, F., Caimano, M., Romania, P., Moretti, M., Lospinoso Severini, L., Talbot, J., Melaiu, O., Tanori, M., et al. (2019). ERAP1 promotes Hedgehog-dependent tumorigenesis by controlling USP47-mediated degradation of βTrCP. Nat. Commun. *10*, 3304. https://doi.org/10.1038/s41467-019-11093-0.
22. D'Amico, S., Tempora, P., Melaiu, O., Lucarini, V., Cifaldi, L., Locatelli, F., and Fruci, D. (2022). Targeting the antigen processing and presentation pathway to overcome resistance to immune checkpoint therapy. Front. Immunol. *13*, 948297. https://doi.org/10.3389/fimmu.2022.948297.
23. López de Castro, J.A. (2018). How ERAP1 and ERAP2 Shape the Peptidomes of Disease-Associated MHC-I Proteins. Front. Immunol. *9*, 2463. https://doi.org/10.3389/fimmu.2018.02463.
24. Bufalieri, F., Fruci, D., and Di Marcotullio, L. (2022). ERAP1 as an emerging therapeutic target for medulloblastoma. Trends Cancer *8*, 4–8. https://doi.org/10.1016/j.trecan.2021.09.005.
25. Fougiaxis, V., He, B., Khan, T., Vatinel, R., Koutroumpa, N.M., Afantitis, A., Lesire, L., Sierocki, P., Deprez, B., and Deprez-Poulain, R. (2024). ERAP Inhibitors in Autoimmunity and Immuno-Oncology: Medicinal Chemistry Insights. J. Med. Chem. *67*, 11597–11621. https://doi.org/10.1021/acs.jmedchem.4c00840.
26. Haynes, H., Nelson, E., and Price, J. (1952). Alkaloids of the Australian Rutaceae: Pentaceras australis Hook. F. I. Isolation of the Alkaloids and Identification of Canthin-6-one. Aust. J. Chem. *5*, 387. https://doi.org/10.1071/CH9520387.
27. Ascher, D.B., Polekhina, G., and Parker, M.W. (2012). Crystallization and preliminary X-ray diffraction analysis of human endoplasmic reticulum aminopeptidase 2. Acta Crystallogr. F Struct. Biol. Cryst. Commun. *68*, 468–471. https://doi.org/10.1107/S1744309112006963.
28. Ghirga, F., Quaglio, D., Mori, M., Cammarone, S., Iazzetti, A., Goggiamani, A., Ingallina, C., Botta, B., and Calcaterra, A. (2021). A unique high-diversity natural product collection as a reservoir of new therapeutic leads. Org. Chem. Front. *8*, 996–1025. https://doi.org/10.1039/D0QO01210F.
29. Ran (2005). Study on Pharmacokinetics of p-Coumaric Acid in Baihuasheshecao Injection. Chin. J. Pharm. Anal. *25*, 759–761.
30. Monache, F.D., Mc Quhae, M.M., Ferrari, F., and Marini-Bettolo, G.B. (1979). Ferruginin A and B and ferruanthrone, new triprenylated anthranoids from Vismia baccifera var. ferruginea. Tetrahedron *35*, 2143–2149. https://doi.org/10.1016/0040-4020(79)87031-3.
31. Sawaya, A.C.H.F., Vaz, B.G., Eberlin, M.N., and Mazzafera, P. (2011). Screening species of Pilocarpus (Rutaceae) as sources of pilocarpine and other imidazole alkaloids. Genet. Resour. Crop Evol. *58*, 471–480. https://doi.org/10.1007/s10722-011-9660-2.
32. Barbosa, L.F., Braz-Filho, R., and Vieira, I.J.C. (2011). Chemical Constituents of Plants from the Genus *Simaba* (Simaroubaceae). Chem. Biodivers. *8*, 2163–2178. https://doi.org/10.1002/cbdv.201000323.
33. Pollier, J., and Goossens, A. (2012). Oleanolic acid. Phytochemistry *77*, 10–15. https://doi.org/10.1016/j.phytochem.2011.12.022.
34. Laphookhieo, S., Phungpanya, C., Tantapakul, C., Techa, S., Tha-in, S., and Narmdorkmai, W. (2012). Chemical constituents from Aegle marmelos. J. Braz. Chem. Soc. *22*, 176–178. https://doi.org/10.1590/S0103-50532011000100024.
35. Karthikeyan, R., Devadasu, C., and Srinivasa Babu, P. (2015). Isolation, Characterization, and RP-HPLC Estimation of P-Coumaric Acid from Methanolic Extract of Durva Grass (*Cynodon dactylon* Linn.) (Pers.). Int. J. Anal. Chem. *2015*, 201386. https://doi.org/10.1155/2015/201386.
36. Zhou, Y.-X., Xia, W., Yue, W., Peng, C., Rahman, K., and Zhang, H. (2015). Rhein: A Review of Pharmacological Activities. Evid. Based. Complement. Alternat. Med. *2015*, 578107. https://doi.org/10.1155/2015/578107.
37. Kim, H.-J., Seo, Y.-J., Htwe, K.-M., and Yoon, K.-D. (2021). Chemical Constituents from Aegle marmelos Fruits. nps. *27*, 240–249. https://doi.org/10.20307/nps.2021.27.4.240.
38. Płowuszyńska, A., and Gliszczyńska, A. (2021). Recent Developments in Therapeutic and Nutraceutical Applications of p-Methoxycinnamic Acid from Plant Origin. Molecules *26*, 3827. https://doi.org/10.3390/molecules26133827.
39. Farouil, L., Sylvestre, M., Fournet, A., and Cebrián-Torrejón, G. (2022). Review on canthin-6-one alkaloids: Distribution, chemical aspects and biological activities. Eur. J. Med. Chem. Rep. *5*, 100049. https://doi.org/10.1016/j.ejmcr.2022.100049.

40. Muruganathan, N., Dhanapal, A.R., Baskar, V., Muthuramalingam, P., Selvaraj, D., Aara, H., Shiek Abdullah, M.Z., and Sivanesan, I. (2022). Recent Updates on Source, Biosynthesis, and Therapeutic Potential of Natural Flavonoid Luteolin: A Review. Metabolites *12*, 1145. https://doi.org/10.3390/metabo12111145.

41. Kumari, M., Radha, Kumar, M., Kumar, M., Zhang, B., Amarowicz, R., Puri, S., Pundir, A., Rathour, S., Kumari, N., et al. (2022). Acacia catechu (L.f.) Willd.: A Review on Bioactive Compounds and Their Health Promoting Functionalities. Plants *11*, 3091. https://doi.org/10.3390/plants11223091.

42. Thakar, S.R., Dhamade, P.N., and Bansode, D.A. (2023). CINNAMIC ACID AND ITS DERIVATIVES AS POTENTIAL ANTI-TUBERCULAR AGENTS. IND. DRU. *60*, 7–19. https://doi.org/10.53879/id.60.12.12905.

43. Towne, C.F., York, I.A., Neijssen, J., Karow, M.L., Murphy, A.J., Valenzuela, D.M., Yancopoulos, G.D., Neefjes, J.J., and Rock, K.L. (2005). Leucine Aminopeptidase Is Not Essential for Trimming Peptides in the Cytosol or Generating Epitopes for MHC Class I Antigen Presentation. J. Immunol. *175*, 6605–6614. https://doi.org/10.4049/jimmunol.175.10.6605.

44. York, I.A., Brehm, M.A., Zendzian, S., Towne, C.F., and Rock, K.L. (2006). Endoplasmic reticulum aminopeptidase 1 (ERAP1) trims MHC class I-presented peptides *in vivo* and plays an important role in immunodominance. Proc. Natl. Acad. Sci. USA *103*, 9202–9207. https://doi.org/10.1073/pnas.0603095103.

45. James, E., Bailey, I., Sugiyarto, G., and Elliott, T. (2013). Induction of Protective Antitumor Immunity through Attenuation of ERAAP Function. J. Immunol. *190*, 5839–5846. https://doi.org/10.4049/jimmunol.1300220.

46. Cifaldi, L., Romania, P., Falco, M., Lorenzi, S., Meazza, R., Petrini, S., Andreani, M., Pende, D., Locatelli, F., and Fruci, D. (2015). ERAP1 regulates natural killer cell function by controlling the engagement of inhibitory receptors. Cancer Res. *75*, 824–834. https://doi.org/10.1158/0008-5472.CAN-14-1643.

47. Hryczanek, R.P., Hackett, A.S., Rowland, P., Chung, C.W., Convery, M.A., Holmes, D.S., Hutchinson, J.P., Kitchen, S., Korczynska, J., Law, R.P., et al. (2024). Optimization of Potent and Selective Cyclohexyl Acid ERAP1 Inhibitors Using Structure- and Property-Based Drug Design. ACS Med. Chem. Lett. *15*, 2107–2114. https://doi.org/10.1021/acsmedchemlett.4c00401.

48. Axelsson, H., Almqvist, H., Seashore-Ludlow, B., and Lundbäck, T. (2004). Screening for Target Engagement using the Cellular Thermal Shift Assay - CETSA. In Assay Guidance Manual, S. Markossian, A. Grossman, M. Arkin, D. Auld, C. Austin, J. Baell, K. Brimacombe, T.D.Y. Chung, N.P. Coussens, and J.L. Dahlin, et al., eds. (Eli Lilly & Company and the National Center for Advancing Translational Sciences).

49. Taipale, J., Chen, J.K., Cooper, M.K., Wang, B., Mann, R.K., Milenkovic, L., Scott, M.P., and Beachy, P.A. (2000). Effects of oncogenic mutations in Smoothened and Patched can be reversed by cyclopamine. Nature *406*, 1005–1009. https://doi.org/10.1038/35023008.

50. Chen, J.K., Taipale, J., Cooper, M.K., and Beachy, P.A. (2002). Inhibition of Hedgehog signaling by direct binding of cyclopamine to Smoothened. Genes Dev. *16*, 2743–2748. https://doi.org/10.1101/gad.1025302.

51. Goodrich, L.V., Milenković, L., Higgins, K.M., and Scott, M.P. (1997). Altered Neural Cell Fates and Medulloblastoma in Mouse *patched* Mutants. Science *277*, 1109–1113. https://doi.org/10.1126/science.277.5329.1109.

52. Kochan, G., Krojer, T., Harvey, D., Fischer, R., Chen, L., Vollmar, M., Von Delft, F., Kavanagh, K.L., Brown, M.A., Bowness, P., et al. (2011). Crystal structures of the endoplasmic reticulum aminopeptidase-1 (ERAP1) reveal the molecular basis for N-terminal peptide trimming. Proc. Natl. Acad. Sci. USA *108*, 7745–7750. https://doi.org/10.1073/pnas.1101262108.

53. Nguyen, T.T., Chang, S.-C., Evnouchidou, I., York, I.A., Zikos, C., Rock, K.L., Goldberg, A.L., Stratikos, E., and Stern, L.J. (2011). Structural basis for antigenic peptide precursor processing by the endoplasmic reticulum aminopeptidase ERAP1. Nat. Struct. Mol. Biol. *18*, 604–613. https://doi.org/10.1038/nsmb.2021.

54. Wechsler-Reya, R.J., and Scott, M.P. (1999). Control of Neuronal Precursor Proliferation in the Cerebellum by Sonic Hedgehog. Neuron *22*, 103–114. https://doi.org/10.1016/S0896-6273(00)80682-0.

55. Schüller, U., Heine, V.M., Mao, J., Kho, A.T., Dillon, A.K., Han, Y.-G., Huillard, E., Sun, T., Ligon, A.H., Qian, Y., et al. (2008). Acquisition of Granule Neuron Precursor Identity Is a Critical Determinant of Progenitor Cell Competence to Form Shh-Induced Medulloblastoma. Cancer Cell *14*, 123–134. https://doi.org/10.1016/j.ccr.2008.07.005.

56. Yang, C., Zhan, H., Zhao, Y., Wu, Y., Li, L., and Wang, H. (2021). MEX3A contributes to development and progression of glioma through regulating cell proliferation and cell migration and targeting CCL2. Cell Death Dis. *12*, 14. https://doi.org/10.1038/s41419-020-03307-x.

57. Yan, J., Parekh, V.V., Mendez-Fernandez, Y., Olivares-Villagómez, D., Dragovic, S., Hill, T., Roopenian, D.C., Joyce, S., and Van Kaer, L. (2006). In vivo role of ER-associated peptidase activity in tailoring peptides for presentation by MHC class Ia and class Ib molecules. J. Exp. Med. *203*, 647–659. https://doi.org/10.1084/jem.20052271.

58. Neumann, J.E., Swartling, F.J., and Schüller, U. (2017). Medulloblastoma: experimental models and reality. Acta Neuropathol. *134*, 679–689. https://doi.org/10.1007/s00401-017-1753-3.

59. Kumar, L.P., Deepa, S.F.A.J., Moinca, I., Suresh, P., and Naidu, K.V.J.R. (2015). Medulloblastoma: A common pediatric tumor: Prognostic factors and predictors of outcome. Asian J. Neurosurg. *10*, 50. https://doi.org/10.4103/1793-5482.151516.

60. Hayden Gephart, M.G., Su, Y.S., Bandara, S., Tsai, F.-C., Hong, J., Conley, N., Rayburn, H., Milenkovic, L., Meyer, T., and Scott, M.P. (2013). Neuropilin-2 contributes to tumorigenicity in a mouse model of Hedgehog pathway medulloblastoma. J. Neurooncol. *115*, 161–168. https://doi.org/10.1007/s11060-013-1216-1.

61. Tang, Y., Gholamin, S., Schubert, S., Willardson, M.I., Lee, A., Bandopadhayay, P., Bergthold, G., Masoud, S., Nguyen, B., Vue, N., et al. (2014). Epigenetic targeting of Hedgehog pathway transcriptional output through BET bromodomain inhibition. Nat. Med. *20*, 732–740. https://doi.org/10.1038/nm.3613.

62. Aszterbaum, M., Epstein, J., Oro, A., Douglas, V., LeBoit, P.E., Scott, M.P., and Epstein, E.H. (1999). Ultraviolet and ionizing radiation enhance the growth of BCCs and trichoblastomas in patched heterozygous knockout mice. Nat. Med. *5*, 1285–1291. https://doi.org/10.1038/15242.

63. Infante, P., Mori, M., Alfonsi, R., Ghirga, F., Aiello, F., Toscano, S., Ingallina, C., Siler, M., Cucchi, D., Po, A., et al. (2015). Gli1/DNA interaction is a druggable target for Hedgehog-dependent tumors. EMBO J. *34*, 200–217. https://doi.org/10.15252/embj.201489213.

64. Yang, Z.-J., Ellis, T., Markant, S.L., Read, T.-A., Kessler, J.D., Bourboulas, M., Schüller, U., Machold, R., Fishell, G., Rowitch, D.H., et al. (2008). Medulloblastoma Can Be Initiated by Deletion of Patched in Lineage-Restricted Progenitors or Stem Cells. Cancer Cell *14*, 135–145. https://doi.org/10.1016/j.ccr.2008.07.003.

65. Sasai, K., Romer, J.T., Lee, Y., Finkelstein, D., Fuller, C., McKinnon, P.J., and Curran, T. (2006). Shh Pathway Activity Is Down-Regulated in Cultured Medulloblastoma Cells: Implications for Preclinical Studies. Cancer Res. *66*, 4215–4222. https://doi.org/10.1158/0008-5472.can-05-4505.

66. Manoranjan, B., Venugopal, C., McFarlane, N., Doble, B.W., Dunn, S.E., Scheinemann, K., and Singh, S.K. (2013). Medulloblastoma stem cells: Modeling tumor heterogeneity. Cancer Lett. *338*, 23–31. https://doi.org/10.1016/j.canlet.2012.07.010.

67. Justilien, V., and Fields, A.P. (2015). Molecular Pathways: Novel Approaches for Improved Therapeutic Targeting of Hedgehog Signaling in Cancer Stem Cells. Clin. Cancer Res. *21*, 505–513. https://doi.org/10.1158/1078-0432.CCR-14-0507.

68. Cochrane, C.R., Szczepny, A., Watkins, D.N., and Cain, J.E. (2015). Hedgehog Signaling in the Maintenance of Cancer Stem Cells. Cancers *7*, 1554–1585. https://doi.org/10.3390/cancers7030851.

69. Chen, K., Huang, Y.h., and Chen, J.l. (2013). Understanding and targeting cancer stem cells: therapeutic implications and challenges. Acta Pharmacol. Sin. *34*, 732–740. https://doi.org/10.1038/aps.2013.27.

70. Grausam, K.B., Dooyema, S.D.R., Bihannic, L., Premathilake, H., Morrissy, A.S., Forget, A., Schaefer, A.M., Gundelach, J.H., Macura, S., Maher, D.M., et al. (2017). ATOH1 Promotes Leptomeningeal Dissemination and Metastasis of Sonic Hedgehog Subgroup Medulloblastomas. Cancer Res. *77*, 3766–3777. https://doi.org/10.1158/0008-5472.CAN-16-1836.

71. Robarge, K.D., Brunton, S.A., Castanedo, G.M., Cui, Y., Dina, M.S., Goldsmith, R., Gould, S.E., Guichert, O., Gunzner, J.L., Halladay, J., et al. (2009). GDC-0449—A

potent inhibitor of the hedgehog pathway. Bioorg. Med. Chem. Lett. *19*, 5576–5581. https://doi.org/10.1016/j.bmcl.2009.08.049.

72. Valenzuela, M., Glorieux, C., Stockis, J., Sid, B., Sandoval, J.M., Felipe, K.B., Kviecinski, M.R., Verrax, J., and Buc Calderon, P. (2014). Retinoic acid synergizes ATO-mediated cytotoxicity by precluding Nrf2 activity in AML cells. Br. J. Cancer *111*, 874–882. https://doi.org/10.1038/bjc.2014.380.
73. Quinlan, A., and Rizzolo, D. (2017). Understanding medulloblastoma. JAAPA *30*, 30–36. https://doi.org/10.1097/01.JAA.0000524717.71084.50.
74. Louis, D.N., Perry, A., Wesseling, P., Brat, D.J., Cree, I.A., Figarella-Branger, D., Hawkins, C., Ng, H.K., Pfister, S.M., Reifenberger, G., et al. (2021). The 2021 WHO Classification of Tumors of the Central Nervous System: a summary. Neuro. Oncol. *23*, 1231–1251. https://doi.org/10.1093/neuonc/noab106.
75. Rimkus, T.K., Carpenter, R.L., Qasem, S., Chan, M., and Lo, H.-W. (2016). Targeting the Sonic Hedgehog Signaling Pathway: Review of Smoothened and GLI Inhibitors. Cancers *8*, 22. https://doi.org/10.3390/cancers8020022.
76. Liu, K.-W., Pajtler, K.W., Worst, B.C., Pfister, S.M., and Wechsler-Reya, R.J. (2017). Molecular mechanisms and therapeutic targets in pediatric brain tumors. Sci. Signal. *10*, eaaf7593. https://doi.org/10.1126/scisignal.aaf7593.
77. Lospinoso Severini, L., Loricchio, E., Navacci, S., Basili, I., Alfonsi, R., Bernardi, F., Moretti, M., Conenna, M., Cucinotta, A., Coni, S., et al. (2024). SALL4 is a CRL3REN/KCTD11 substrate that drives Sonic Hedgehog-dependent medulloblastoma. Cell Death Differ. *31*, 170–187. https://doi.org/10.1038/s41418-023-01246-6.
78. Reeves, E., Islam, Y., and James, E. (2020). ERAP1: a potential therapeutic target for a myriad of diseases. Expert Opin. Ther. Targets *24*, 535–544. https://doi.org/10.1080/14728222.2020.1751821.
79. Cifaldi, L., Lo Monaco, E., Forloni, M., Giorda, E., Lorenzi, S., Petrini, S., Tremante, E., Pende, D., Locatelli, F., Giacomini, P., and Fruci, D. (2011). Natural Killer Cells Efficiently Reject Lymphoma Silenced for the Endoplasmic Reticulum Aminopeptidase Associated with Antigen Processing. Cancer Res. *71*, 1597–1606. https://doi.org/10.1158/0008-5472.CAN-10-3326.
80. Patridge, E., Gareiss, P., Kinch, M.S., and Hoyer, D. (2016). An analysis of FDA-approved drugs: natural products and their derivatives. Drug Discov. Today *21*, 204–207. https://doi.org/10.1016/j.drudis.2015.01.009.
81. Scales, S.J., and De Sauvage, F.J. (2009). Mechanisms of Hedgehog pathway activation in cancer and implications for therapy. Trends Pharmacol. Sci. *30*, 303–312. https://doi.org/10.1016/j.tips.2009.03.007.
82. Lospinoso Severini, L., Ghirga, F., Bufalieri, F., Quaglio, D., Infante, P., and Di Marcotullio, L. (2020). The SHH/GLI signaling pathway: a therapeutic target for medulloblastoma. Expert Opin. Ther. Targets *24*, 1159–1181. https://doi.org/10.1080/14728222.2020.1823967.
83. Yuan, N.-N., Cai, C.-Z., Wu, M.-Y., Zhu, Q., Su, H., Li, M., Ren, J., Tan, J.-Q., and Lu, J.-H. (2019). Canthin-6-One Accelerates Alpha-Synuclein Degradation by Enhancing UPS Activity: Drug Target Identification by CRISPR-Cas9 Whole Genome-Wide Screening Technology. Front. Pharmacol. *10*, 16. https://doi.org/10.3389/fphar.2019.00016.
84. Torquato, H.F.V., Junior, M.T.R., Lima, C.S., Júnior, R.T.D.A., Talhati, F., Dias, D. A., Justo, G.Z., Ferreira, A.T., Pilli, R.A., and Paredes-Gamero, E.J. (2022). A canthin-6-one derivative induces cell death by apoptosis/necroptosis-like with DNA damage in acute myeloid cells. Biomed. Pharmacother. *145*, 112439. https://doi.org/10.1016/j.biopha.2021.112439.
85. Vieira Torquato, H.F., Ribeiro-Filho, A.C., Buri, M.V., Araújo Júnior, R.T., Pimenta, R., De Oliveira, J.S.R., Filho, V.C., Macho, A., Paredes-Gamero, E.J., and De Oliveira Martins, D.T. (2017). Canthin-6-one induces cell death, cell cycle arrest and differentiation in human myeloid leukemia cells. Biochim. Biophys. Acta Gen. Subj. *1861*, 958–967. https://doi.org/10.1016/j.bbagen.2017.01.033.
86. Zhang, Z., Wang, A., Wang, Y., Sun, W., Zhou, X., Xu, Q., Mao, L., and Zhang, J. (2023). Canthin-6-Ones: Potential Drugs for Chronic Inflammatory Diseases by Targeting Multiple Inflammatory Mediators. Molecules *28*, 3381. https://doi.org/10.3390/molecules28083381.
87. Tian, J., Shen, Y., Li, H., Liu, R., Shan, L., Gao, J., and Zhang, W. (2012). Carboline Alkaloids from *Psammosilene tunicoides* and Their Cytotoxic Activities. Planta Med. *78*, 625–629. https://doi.org/10.1055/s-0031-1298322.
88. Dejos, C., Voisin, P., Bernard, M., Régnacq, M., and Bergès, T. (2014). Canthin-6-one Displays Antiproliferative Activity and Causes Accumulation of Cancer Cells in the G2/M Phase. J. Nat. Prod. *77*, 2481–2487. https://doi.org/10.1021/np500516v.
89. McGann, M. (2011). FRED Pose Prediction and Virtual Screening Accuracy. J. Chem. Inf. Model. *51*, 578–596. https://doi.org/10.1021/ci100436p.
90. McGann, M. (2012). FRED and HYBRID docking performance on standardized datasets. J. Comput. Aided. Mol. Des. *26*, 897–906. https://doi.org/10.1007/s10822-012-9584-8.
91. Hawkins, P.C.D., Skillman, A.G., Warren, G.L., Ellingson, B.A., and Stahl, M.T. (2010). Conformer Generation with OMEGA: Algorithm and Validation Using High Quality Structures from the Protein Databank and Cambridge Structural Database. J. Chem. Inf. Model. *50*, 572–584. https://doi.org/10.1021/ci100031x.
92. Choonong, R., Ruangdachsuwan, S., Churod, T., Palabodeewat, S., Punyahathaikul, S., Juntarapornchai, S., Ketsuwan, K., Komaikul, J., Masrinoul, P., Kitisripanya, T., et al. (2022). Evaluating the *in Vitro* Efficacy of Quassinoids from *Eurycoma longifolia* and *Eurycoma harmandiana* against Common Cold Human Coronavirus OC43 and SARS-CoV-2 Using In-Cell Enzyme-Linked Immunosorbent Assay. J. Nat. Prod. *85*, 2779–2788. https://doi.org/10.1021/acs.jnatprod.2c00736.
93. Govindan, B., Johnson, A.J., Viswanathan, G., Ramaswamy, V., Koshy, K.C., and Baby, S. (2019). Secondary metabolites from the unique bamboo, *Melocanna baccifera*. Nat. Prod. Res. *33*, 122–125. https://doi.org/10.1080/14786419.2018.1434647.
94. Park, I., Byun, H.S., Hur, G.M., and Na, M. (2021). Tulipiferamide A, an Alkamide from *Liriodendron tulipifera* , Exhibits an Anti-Inflammatory Effect via Targeting IKKβ Phosphorylation. J. Nat. Prod. *84*, 1598–1606. https://doi.org/10.1021/acs.jnatprod.1c00146.
95. Liu, W.J., Hou, X.Q., Chen, H., Liang, J.Y., and Sun, J.B. (2016). Chemical constituents from *Agrimonia pilosa* Ledeb. and their chemotaxonomic significance. Nat. Prod. Res. *30*, 2495–2499. https://doi.org/10.1080/14786419.2016.1198351.
96. Huang, A.-C., Wilde, A., Ebmeyer, J., Skouroumounis, G.K., and Taylor, D.K. (2013). Examination of the Phenolic Profile and Antioxidant Activity of the Leaves of the Australian Native Plant *Smilax glyciphylla*. J. Nat. Prod. *76*, 1930–1936. https://doi.org/10.1021/np4005163.
97. Yuan, T., Wu, Z., Zhai, S., Wang, R., Wu, S., Cheng, J., Zheng, M., and Wang, X. (2023). Photosynthetic Fixation of CO_2 in Alkenes by Heterogeneous Photoredox Catalysis with Visible Light. Angew. Chem. Int. Ed. *62*, e202304861. https://doi.org/10.1002/anie.202304861.
98. Mishra, T., Gupta, S., Rai, P., Khandelwal, N., Chourasiya, M., Kushwaha, V., Singh, A., Varshney, S., Gaikwad, A.N., and Narender, T. (2023). Anti-adipogenic action of a novel oxazole derivative through activation of AMPK pathway. Eur. J. Med. Chem. *262*, 115895. https://doi.org/10.1016/j.ejmech.2023.115895.
99. Dener, J.M., Zhang, L.H., and Rapoport, H. (1993). An effective chirospecific synthesis of (+)-pilocarpine from L-aspartic acid. J. Org. Chem. *58*, 1159–1166. https://doi.org/10.1021/jo00057a031.
100. Manalastas-Cantos, K., Konarev, P.V., Hajizadeh, N.R., Kikhney, A.G., Petoukhov, M.V., Molodenskiy, D.S., Panjkovich, A., Mertens, H.D.T., Gruzinov, A., Borges, C., et al. (2021). *ATSAS 3.0* : expanded functionality and new tools for small-angle scattering data analysis. J. Appl. Crystallogr. *54*, 343–355. https://doi.org/10.1107/S1600576720013412.
101. Franke, D., and Svergun, D.I. (2009). *DAMMIF* , a program for rapid *ab-initio* shape determination in small-angle scattering. J. Appl. Crystallogr. *42*, 342–346. https://doi.org/10.1107/S0021889809000338.
102. Svergun, D.I. (1992). Determination of the regularization parameter in indirect-transform methods using perceptual criteria. J. Appl. Crystallogr. *25*, 495–503. https://doi.org/10.1107/S0021889892001663.
103. Chiozzi, R.Z., Capriotti, A.L., Cavaliere, C., La Barbera, G., Montone, C.M., Piovesana, S., and Laganà, A. (2018). Label-Free Shotgun Proteomics Approach to Characterize Muscle Tissue from Farmed and Wild European Sea Bass (Dicentrarchus labrax). Food Anal. Methods *11*, 292–301. https://doi.org/10.1007/s12161-017-0999-7.
104. Cerrato, A., Capriotti, A.L., Cavaliere, C., Montone, C.M., Piovesana, S., and Laganà, A. (2022). Novel Aza-Paternò-Büchi Reaction Allows Pinpointing Carbon–Carbon Double Bonds in Unsaturated Lipids by Higher Collisional Dissociation. Anal. Chem. *94*, 13117–13125. https://doi.org/10.1021/acs.analchem.2c02549.